NOAA Technical Memorandum ERL PMEL-46

A SATELLITE STUDY OF OCEAN INTERNAL WAVES

Constance Sawyer

Pacific Marine Environmental Laboratory
Seattle, Washington
March 1983

UNITED STATES
DEPARTMENT OF COMMERCE
Malcolm Baldrige,
Secretary

NATIONAL OCEANIC AND
ATMOSPHERIC ADMINISTRATION
John V. Byrne,
Administrator

Environmental Research
Laboratories
George H. Ludwig
Director

NOTICE

Mention of a commercial company or product does not constitute an endorsement by NOAA Environmental Research Laboratories. Use for publicity or advertising purposes of information from this publication concerning proprietary products or the tests of such products is not authorized.

Contents

A SATELLITE STUDY OF OCEAN INTERNAL WAVES[1]

by Constance Sawyer[2]

ABSTRACT. Ocean internal-wave slicks over the eastern U.S. continental shelf imaged by the satellite Landsat are described and analyzed. This study confirms generation by semidiurnal tides, locates the site of generation at the edge of the continental shelf, and establishes the time of generation near the time of maximum flood current. Characteristics such as wave-packet extent, water depth, and packet lifetime are quantitatively described. The wavelength spectrum derived from spacing of slicks observed near generation is far from a smooth "universal spectrum." The dominant peak at 26 km corresponds to packet spacing, and a second peak near 450 m corresponds to spacing of slicks within packets. The longest within-packet spacing depends on total water depth. The shortest spacing changes with season and so is probably determined by the depth of the upper warm layer.

Slick visibility is discussed in terms of modification of surface-wave amplitude by the near-surface current system of the internal waves. Possible mechanisms are (1) damping of surface waves by film concentrated at current convergences, and (2) damping of surface waves in a parallel current, and (3) amplification in an adverse current. Calculations indicate that the latter mechanism provides a better quantitative description of the observed contrast between slicks and rough bands. Though the derived dependence on sun altitude and windspeed corresponds to some observed characteristics, the simplified theory and average parameters used in this trial application only partially explain the observed latitude distribution of visible slicks.

From uniformly spaced series of packets, and from similar packet images recorded on successive days, the median lifetime of slick packets is found to be two to three tidal cycles, much longer than the time in which waves are expected to disperse or to break. The balance of non-linear terms in the cnoidal solution of the Korteweg-de Vries equation that permits a stable wave profile relates amplitude and wave number in terms of the elliptic parameter, m. Solutions progress from a train of sinusoidal waves at m = 0, through trains of waves with flat crests and widely separated troughs, to the solitary wave of infinite length at m = 1. The cnoidal solution describes the stability and other observed features of the internal waves, but the variable spacing of slicks within a packet demands a more complex description.

---

[1]Contribution number 634 from NOAA's Pacific Marine Environmental Laboratory.

[2]Present address: 903 East Morehead Circle, No. 2L, Boulder, Colorado 80303.

1. Introduction

Although internal-wave slicks have long been observed and recognized from shipboard, the identification of the slicks on Landsat images (figs. 1 and 2) was not anticipated (Apel et al., 1974; Apel et al., 1975a). The identification was verified by observation of thermal fluctuations and of acoustic echoes from a reflecting layer of undulating depth (Apel et al., 1975b; Proni et al., 1978) (fig. 3). A systematic study of available satellite data on the eastern continental shelf of North America from Cape Hatteras to Nova Scotia was presented pictorially by Sawyer and Apel (1977). Further analysis of these data is presented here.

On a Landsat image the internal-wave signature is a series of parallel curved bands, alternately bright and dark (figs. 1, 2). Typically four or five, but on occasion up to thirty pairs of bands, each a few hundred meters broad, form a packet that is often wedge shaped, with band contrast and breadth decreasing toward the narrower, off-shore end. Packets often occur in series of two or three, separated by about 25 km. These main features were explained by Apel et al. (1975a) in terms of linear theory: tidal currents impinging on the continental slope generate internal waves that propagate shoreward with a velocity that increases with wavelength.

The grid spaces in figure 4 are centered on the nominal positions of Landsat images which, in a given day, form a swath, roughly north-south, 85 km wide. The next day's swath is farther west and, at this latitude, overlaps by about one-third the image width. Orbits and image swaths repeat once every 18 days. The data analyzed here were gathered in the summers of 1972, 1973, and 1974.

The next section describes calculations of expected contrast of rough and smooth bands overlying internal waves. These are based on alternative mechanisms: damping of surface waves by a natural oily film that accumulates at convergence of the internal-wave velocity field, and interaction of the internal-wave current with surface waves. The calculations show the influence on contrast of windspeed, background sea radiance, internal-wave current speed, and sun angle (or of latitude and season). Wave-current interaction appears from these calculations to be the more effective mechanism, at least at low latitude, but damping by an oily film may become more important at high

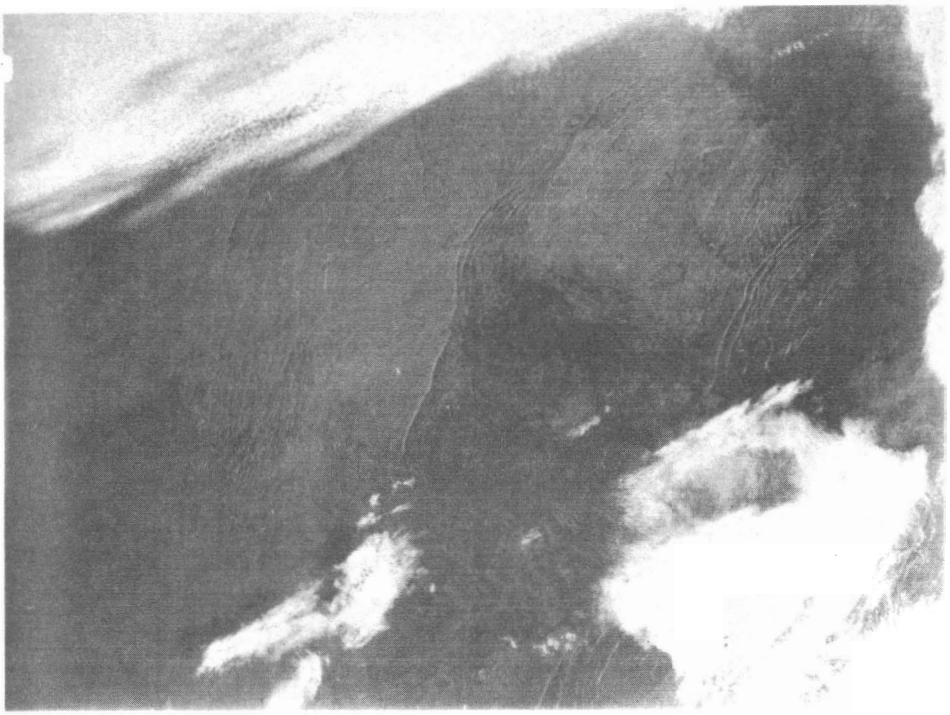

Figure 1. Portion of Landsat image showing internal-wave packets in the Gulf of Maine, 22 July 1973. Clouds appear white and their shadows black. The spacing of the three prominent and similar packets agrees with generation at each semidiurnal tide and a speed of 0.77 ms^{-1}.

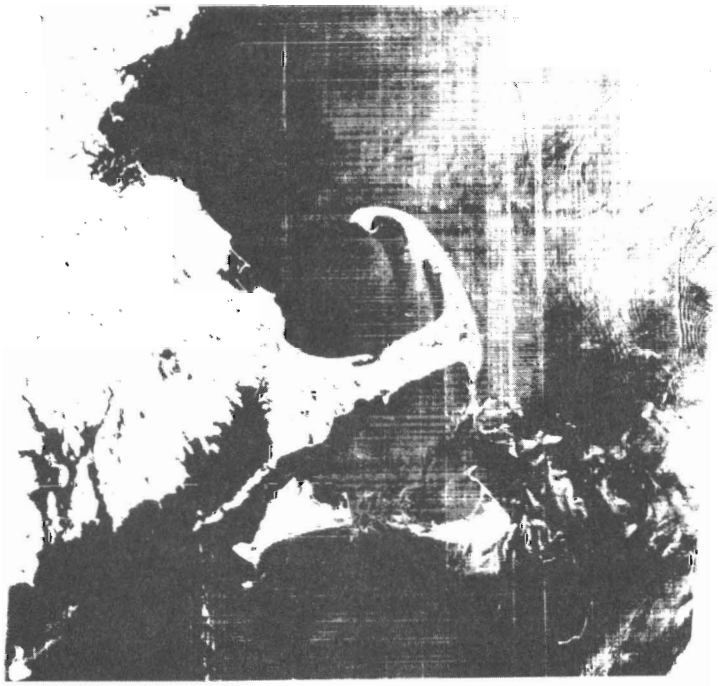

Figure 2. The width of the (negative) photograph corresponds to 84 km. Landsat image for 17 July 1974 showing Cape Cod.

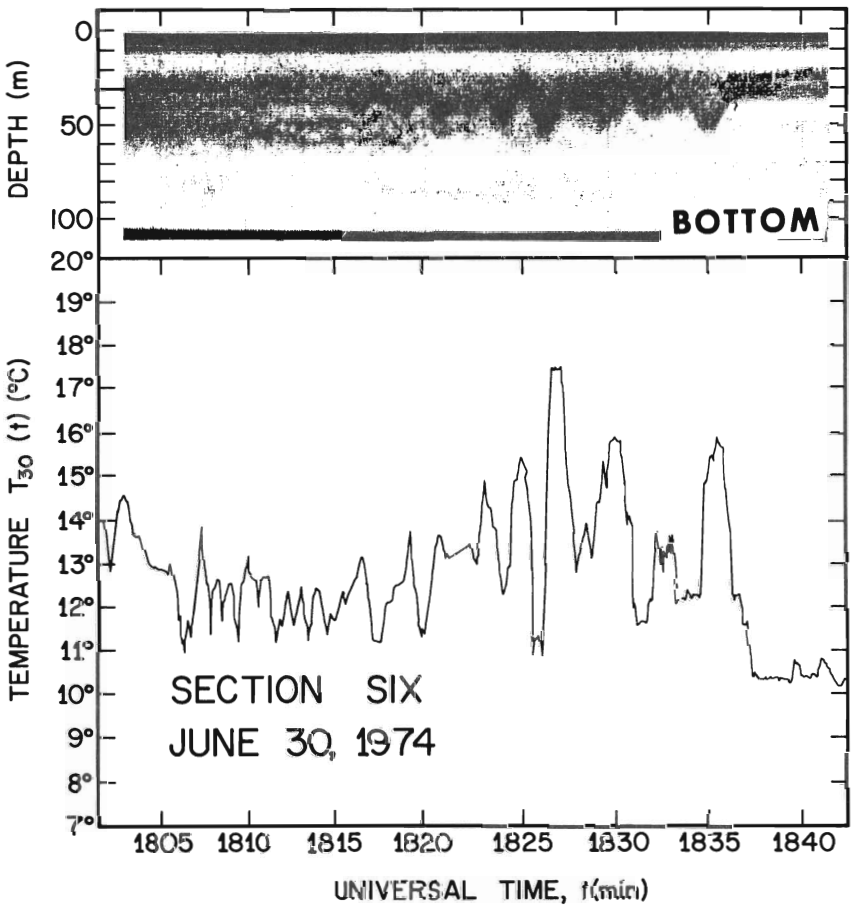

Figure 3. An internal-wave packet observed acoustically (above) and with a thermistor at 30-m depth (below). From Proni, Apel, Byrne, Newman, and Sellers (1978).

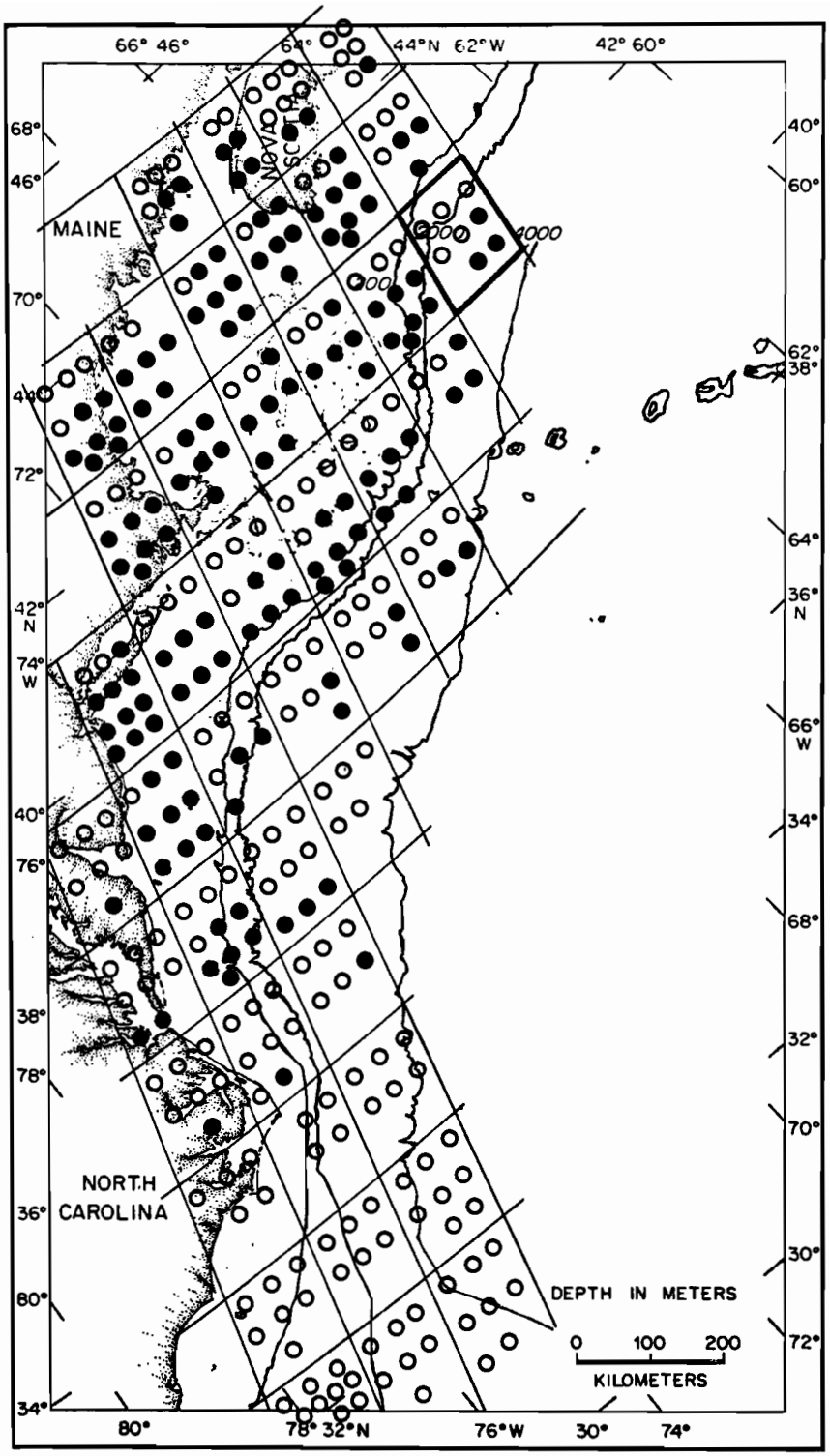

Figure 4. Image swaths and slick statistics on the eastern U.S. continental shelf, summers of 1972, 1973, and 1974 (up to 12 passes at each swath). Each filled circle represents an image on which internal-wave slicks were observed and each open circle an image on which no slicks were found, although the image was at least 50% cloud-free. Images with no slicks and cloud cover more than 50% are not represented. No attempt has been made here to represent the slick position on the image; even though the representative dot may overlie land, the slick was observed on the sea surface (see figure 19).

latitude. The major influence on slick visibility on Landsat images is clouds, discussed in section 3. In section 4, the seasonal change in slick visibility is shown to be due to the seasonal thermocline rather than to seasonal change in sun elevation. Sections 5 through 7 describe various characteristics of internal-wave packets, e.g., their size, number, lifetime, location, and wavelength spectrum. In section 8, the effect of thermocline depth on wavespeed is discussed and wavelengths that appear to measure total depth, as well as thermocline depth, are described. In sections 10 and 11, the long lifetime and slight dispersion of internal-wave packets are shown to be incompatible with linear dispersive waves or with the breaking expected for finite-amplitude waves, or with a train of solitons of varying amplitude. The possibility is discussed of describing the packets as cnoidal waves with elliptic parameter varying within each train. Section 11 discusses evidence that internal waves on the eastern continental shelf of the United States are preferentially generated near flood tide.

2. Visibility of slicks in sun glitter

Two possible mechanisms for producing the alternating rough and smooth bands overlying internal waves are illustrated schematically in figure 5. Though both depend on the internal-wave current, they produce surface slicks that are related differently to the phase of the internal wave. In figure 5 the velocity field of the simplest wave mode is also sketched. The wave profile is similar to profiles observed acoustically (e.g., Proni et al., 1978, p. 78, fig. 33).

Slicks, regions of reduced surface-wave activity, can form as the result of damping of capillary waves by the added surface tension of a natural oil film. Concentration of a surface film at convergences in the horizontal velocity field of the internal wave, with fragmentation of the film at divergences, is one explanation that has been offered for internal-wave slicks; it has been experimentally tested and verified for internal waves off the southern California coast by LaFond and LaFond (1969). Points of convergence and divergence occur over nodes of surface currents in the internal-wave velocity field; concentrated surface film and slicks should be found over the slope following the crest, and rough bands over the slope following the trough. The typical internal-wave profile of figure 5, with the film mechanism, would produce a pattern consisting of a slick, closely followed by a relatively

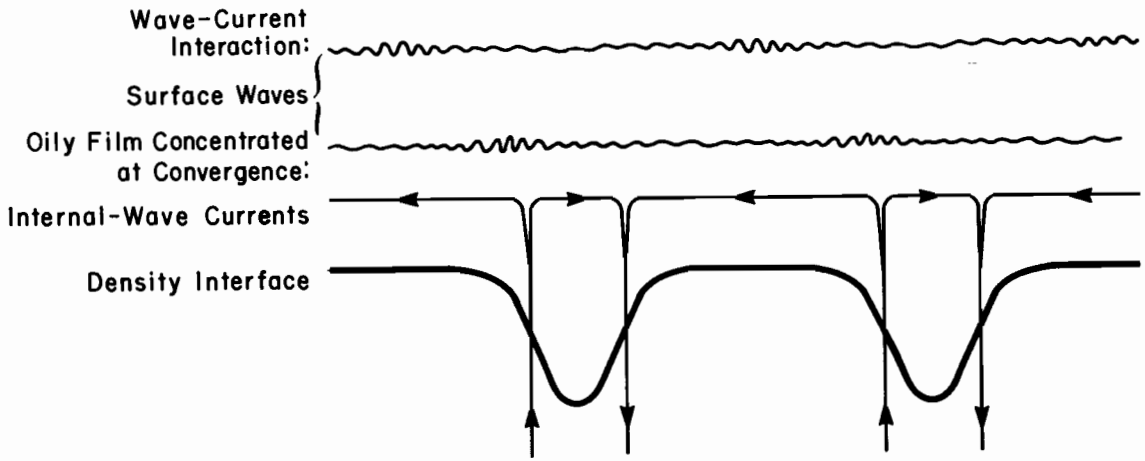

Figure 5. Diagram illustrating the relation of the velocity field of the simplest mode of the internal wave to its profile and showing the expected modulation of surface waves by an oily film concentrated at regions of convergence (lower part) and by direct interaction of surface waves with currents of the internal-wave velocity field (upper part).

rough band, followed by a broad band in which the surface waves are modified only slightly. This latter pattern resembles the intensity pattern seen in some packets with widely spaced bands (for example, the packet at the right-hand edge of fig. 2) with the important difference that the leading band is observed to be bright, which, we shall see, means that it is rough. This does not fit the oily-film picture, in which a slick would be expected at the forward part of the leading trough.

Surface waves can also be modified through direct interaction with currents that form the internal-wave velocity field (Longuet-Higgins and Stewart, 1964). In a parallel current, surface waves are damped and become longer, faster, and flatter while in an adverse current, they become shorter, slower, and steeper. For internal waves of the simplest mode, horizontal velocity near the surface over the trough parallels the direction of propagation and over crests is opposite to the direction of propagation. If the maximum change in surface waves occurs where the current is strongest (the maximum might occur elsewhere if, for example, amplification is so strong that surface waves break) and if wind heading, surface-wave propagation, and internal-wave propagation are all shoreward, rough bands are expected to appear over crests of the internal wave, and slicks over troughs as the surface waves are alternately amplified and damped by interaction with the internal-wave current. Then narrow slicks would appear over the narrow troughs of the typical flat-crested internal wave, and a rough, bright band would lead. These typically observed features fit the interaction picture when wind and surface waves are moving in the same direction as the internal wave. While this is the expected situation (shoreward propagation of internal waves and a sea breeze), there is still no explanation for scenes that show packets that are apparently propagating seaward, as well as shoreward-directed packets, with the bright band leading in both types.

Interpretation of image brightness in terms of roughness of the sea surface, following Cox and Munk (1954), is relatively simple for Landsat geometry (fig. 6). The images of clouds and their shadows show that wherever internal-wave packets are seen, the sea surface is illuminated directly by the sun. Enhanced brightness can be considered as the sum of directly reflected bits of sun images, and as proportional to the sum of areas of sea surfaces with tilt that reflects sunlight to the satellite-borne detector. For sun-

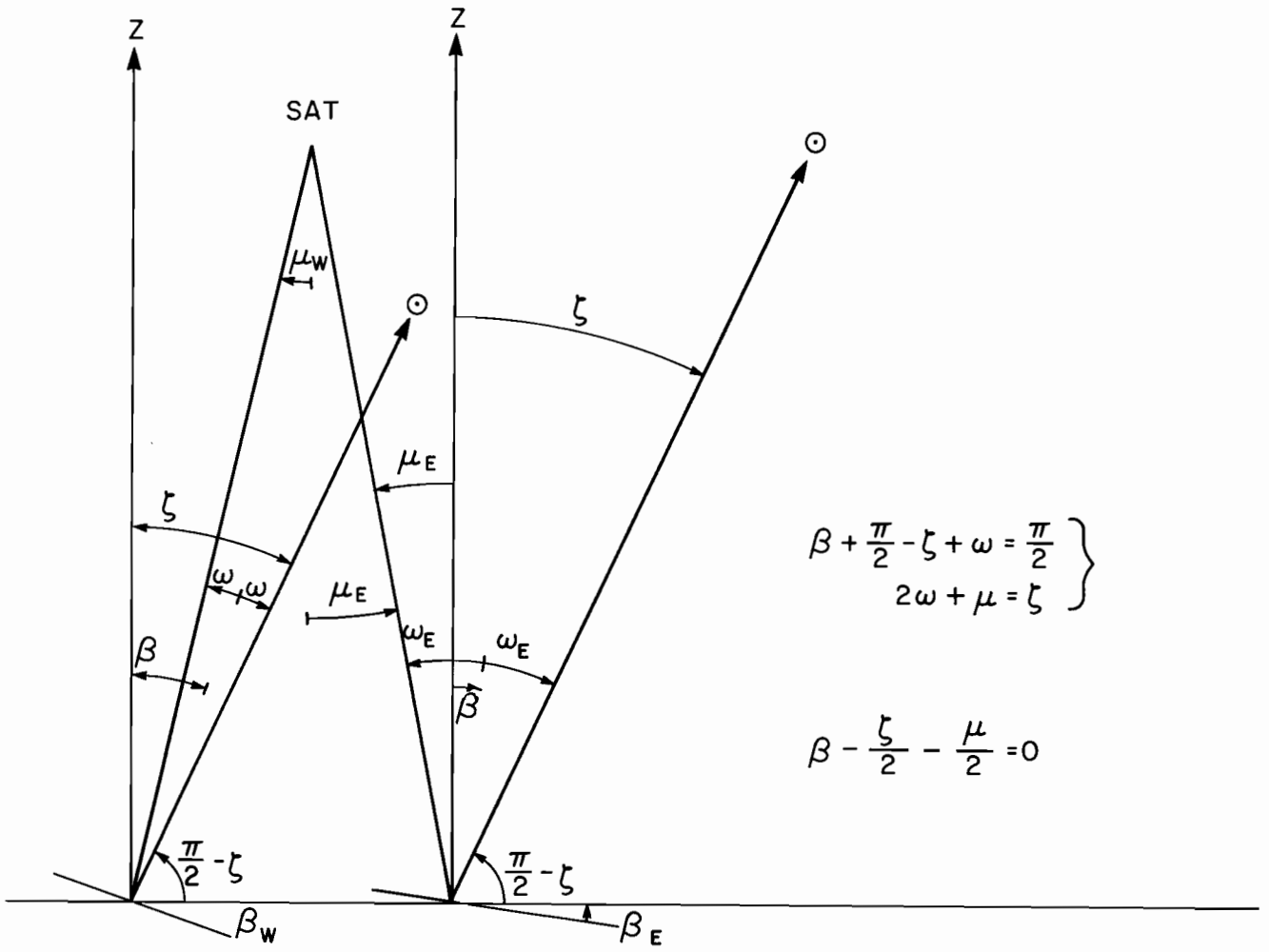

Figure 6. Sketch illustrating tilt β of sea surface for reflection of sunlight to detector at satellite (SAT). The slope is assumed to have no component out of the plane containing the sun, satellite, and reflecting surface. Z is the zenith, θ, the solar direction. Note that μ_E (east) is taken as negative in the expression $\beta = \frac{1}{2}(\zeta + \mu)$.

synchronous Landsat, local time is approximately constant, about 2 hours before noon. Internal-wave slicks were seen in the latitude range 38° to 45°, in summer, when the sun was near its maximum declination of 23.5°. We make the simplifying assumption that steepest ascent of the reflecting surface lies in the vertical plane that contains the detector and the sun, which is oriented (2 hours before local noon) 30° east of the north-south meridian, and approximately normal to the coast line, as one can verify from the map and grid of figure 23. The sun's zenith angle is given by

$$\cos \zeta = \cos (\text{latitude} - \text{sun declination}) \cos (\text{sun azimuth}).$$

With azimuth 30°, declination 21° for the sun, and latitude 40°, $\zeta = 35°$ (sun altitude 55°), a typical value for the images analyzed. Then, if μ is the angle between the vertical and the ray reflected to the detector, measured in the same direction as zenith angle ζ, the tilt for direct reflection is

$$\beta = \tfrac{1}{2} (\zeta + \mu).$$

Over the 185-km breadth of a Landsat image, μ varies within the limits ±5.7° (negative east). For sun zenith angle 35° (altitude 55°), the value of β is 17.5° at the center of the image, 14.6° at the eastern edge, and 20.4° at the western edge. The center of the glitter pattern, from which sunlight is reflected to the detector by a horizontal surface ($\beta = 0°$) lies beyond the eastern limit of the imaged sea surface.

Cox and Munk (1954) show that the occurrence frequency distribution of sea surface slope is close to a normal error distribution, and that the root-mean-squared value of the slope is determined by windspeed. According to their empirical expression for the rms slope:

$$\begin{aligned} \sigma^2 &= 0.003 + 5.12\ 10^{-3}\ W \text{ m/s } \pm 0.004 \text{ in clean water, and} \\ \sigma^2 &= 0.008 + 1.56\ 10^{-3}\ W \text{ m/s } \pm 0.004 \text{ in an oil slick.} \end{aligned} \qquad (1)$$

For reflection of sunlight to the eastern edge of the satellite image, the tilt has its lowest value, 14.6° ($\zeta = 55°$, in sun-satellite-reflection plane). This is beyond the inflection point at $s = \sigma$ in the normal curve if windspeed W is less than 13 m/s, a value near the top of the range included in Cox and Munk's data; thus most slopes that give specular reflection at Landsat lie in the wing of the distribution. The effect of increasing the mean-squared slope σ^2 is to broaden the distribution, decreasing the probability of occurrence of slopes smaller than the rms slope, and increasing the occurrence

frequency of steep slopes. Since specular reflection at the satellite overhead requires a steep slope, a rough surface will look bright on Landsat images.

The photometric gray scale reproduced on Landsat photographic images allows estimates of the relative radiance of bright and dark bands in the packets. Rough estimates made on a Landsat image indicate that the radiance of bright bands can be as large as 6 to 30 times that of dark bands (which are close to the zero end of the gray scale). We ask whether either the damping of short waves by an oily film or the effects of current interaction can lead to values of contrast in this range.

Skewness and kurtosis, and the differences among crosswind, upwind, and downwind spectra are neglected here, and the probability of occurrence of the slope $s_o = \tan \beta_o$ necessary for reflection to the detector is taken as the error function with mean-squared slope defined by (1):

$$P(s_o) = \frac{1}{(2\pi)^{\frac{1}{2}} \sigma} \exp\ (-s_o^2/2\sigma^2) \tag{2}$$

The slope s_o is always taken in this calculation to be tan 17.5°, corresponding to sun elevation of 55°, azimuth 30°E, and reflected ray in the sun-satellite-reflector plane.

A. Wave-Current Interaction

The theory of radiation stress and its effect on surface waves interacting with a mean current has been developed by Longuet-Higgins and Stewart (1964). From their work one can find the amplitude and wavelength, hence the slope of a surface wave with wave speed c in a mean current U.

From their expressions (4) and (5) in §7,

$$\frac{c_i}{c_o} = \tfrac{1}{2}\ (1 \pm (1 + \frac{4U}{c_o})^{\frac{1}{2}}) \tag{3}$$

where the subscript o represents the value of the parameter in the absence of a mean current. $U/c_o > 0$ gives enhanced speed and reduced slope corresponding to a slick (subscript i = S); while for $\frac{U}{c} < 0$, i = R, representing steepened slope and a rough sea. From Longuet-Higgins and Stewart's equation (9), the relative amplitude and energy are given by:

$$\frac{a_i^2}{a_o^2} = \frac{E_i}{E_o} = \left(\frac{c_i}{c_o}\right)^{-2} \left(\frac{2c_i}{c_o} - 1\right)^{-1} \tag{4}$$

and the relative wavelength is given by their equation (5):

$$\lambda_i/\lambda_o = \frac{c_i^2}{c_o^2} \quad . \tag{5}$$

The ratio of steepnesses is,

$$\gamma_i = \frac{s_i}{s_o} = \left(\frac{c_i}{c_o}\right)^{-3} \left(\frac{2c_i}{c_o} - 1\right)^{-\frac{1}{2}} \quad . \tag{6}$$

The change in slope, a function of U/c_o, is shown, along with variations of wave speed, wavelength, and amplitude, in figure 7. When each slope is changed by the factor s_i/s_o, the root-mean-squared slope σ is changed by the same factor, so $\sigma_i = \gamma_i \sigma$. For this analysis, U is the surface current of the internal-wave velocity field, alternately parallel and antiparallel to the direction of propagation of the surface waves. The probability P_i that sunlight is reflected to the detector is computed from the error function, eq. (2) with $\sigma_R = \sigma(W)\ \gamma_R$ for rough bands and $\sigma_S = \sigma(W)\ \gamma_S$ for smooth. The contrast P_R/P_S, is plotted in figure 8 as a function of windspeed for a number of values of mean current, U. When mean current and windspeed are both large, σ_R exceeds s_o, the slope for specular reflection. In this case, further increase of σ_R decreases the probability of occurrence of slope s_o, decreasing the brightness of the rough band, and the ratio of its brightness to the corresponding dark band. Thus, when windspeed is large and mean-squared slope greatly exceeds the slope necessary for reflection, contrast falls with increasing mean current as seen for $\frac{U}{c_o} = 0.24$ and $W > 7\ ms^{-1}$ in figure 8. This effect is illustrated more clearly in figures 9 and 10, where contours of constant P_i are plotted as a function of windspeed and scaled current speed. In a slick (fig. 9a), σ_s is small, so $\frac{s}{\sigma}$ is always large and the necessary slope lies in the wing of the distribution; then P_S is small, and always increases as σ_S increases with increasing windspeed or with decreasing current speed (increasing γ). In figure 9b, $\sigma_R = s_o$ along the dashed line. For values of U and W below this line $\sigma_R < s_o$ and $P_R\ (s_o)$ increases as σ_R increases. For larger values of U, W, and σ_R, $\sigma_R > s_o$, and P_R decreases as σ_R

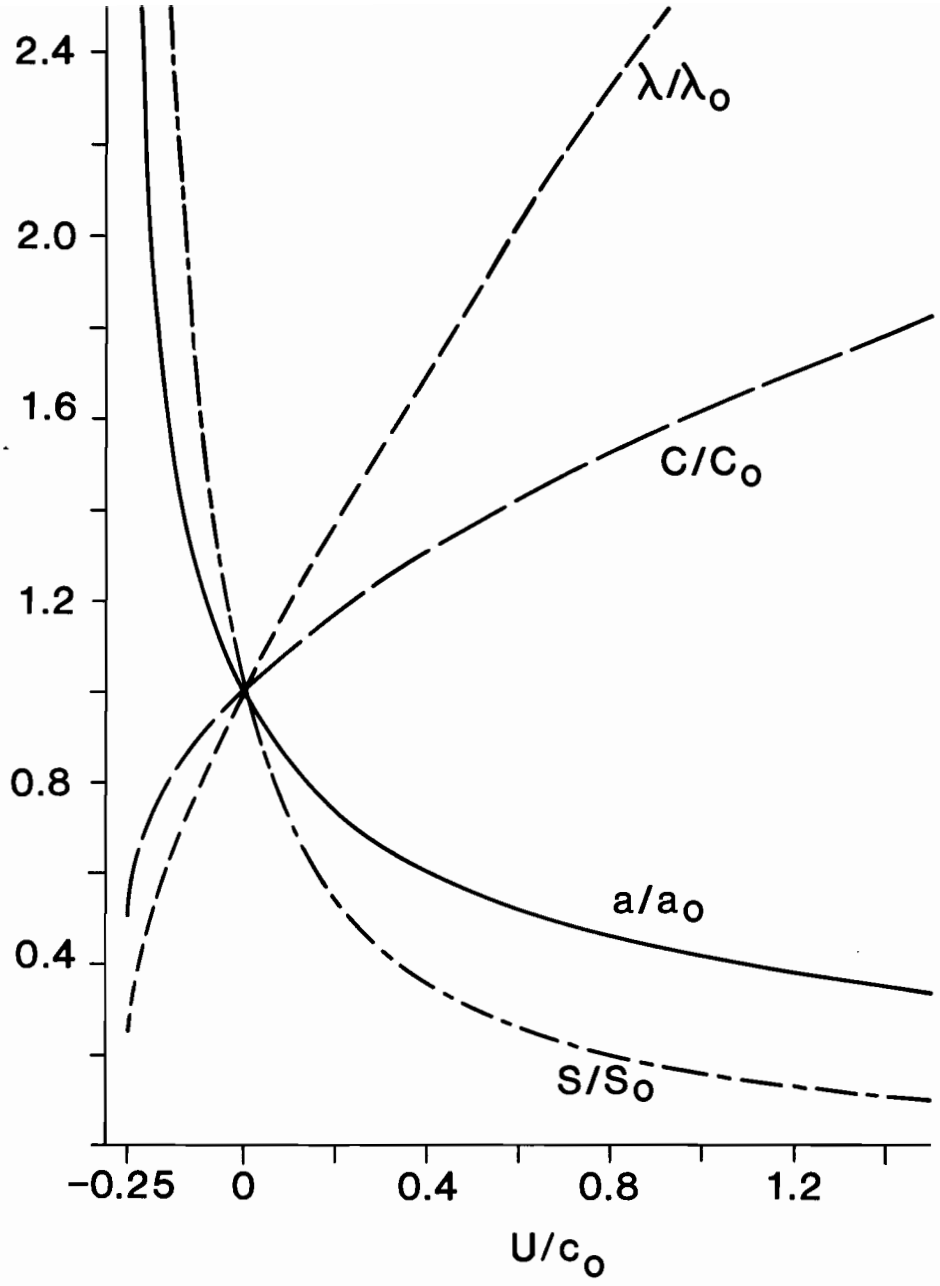

Figure 7. Effects of a mean current on the length, λ, speed, c, amplitude, a, and slope, s, of surface waves according to Longuet-Higgins and Stewart (1964). Each quantity is scaled by its value in the absence of a mean current.

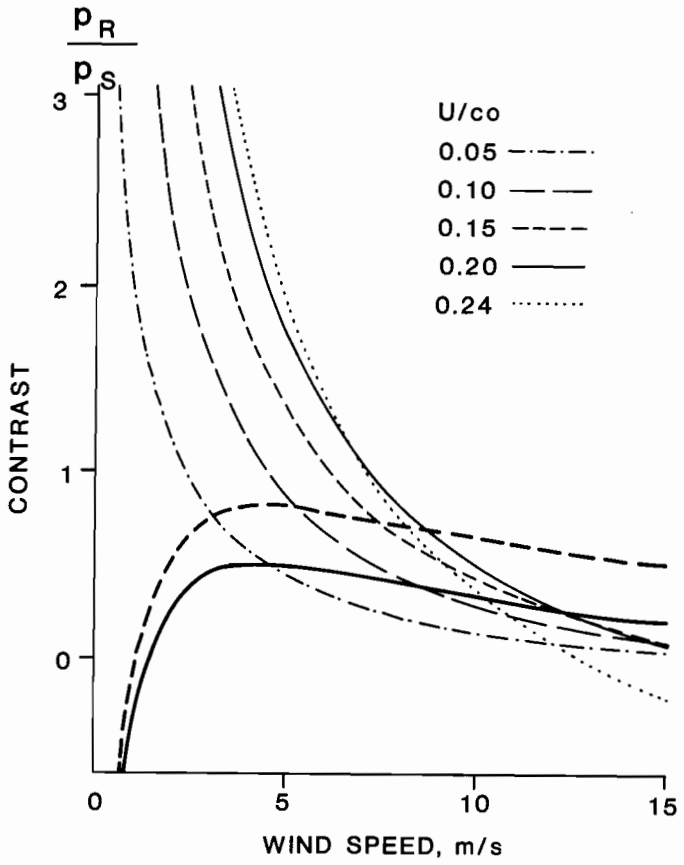

Figure 8. The ratio of probability of occurrence of the sea surface slope necessary for specular reflection of the sun at the center of a Landsat image, for rough bands and for slicks. The curves that go to zero at small windspeed, W, are calculated for an oily slick. The dashed line gives values double those of the continuous line, which represents the difference between the absence and presence of artifically introduced oil. The curves that go to large values of the ratio at small values of windspeed represent the effect of interaction of surface waves with the current system of an internal wave.

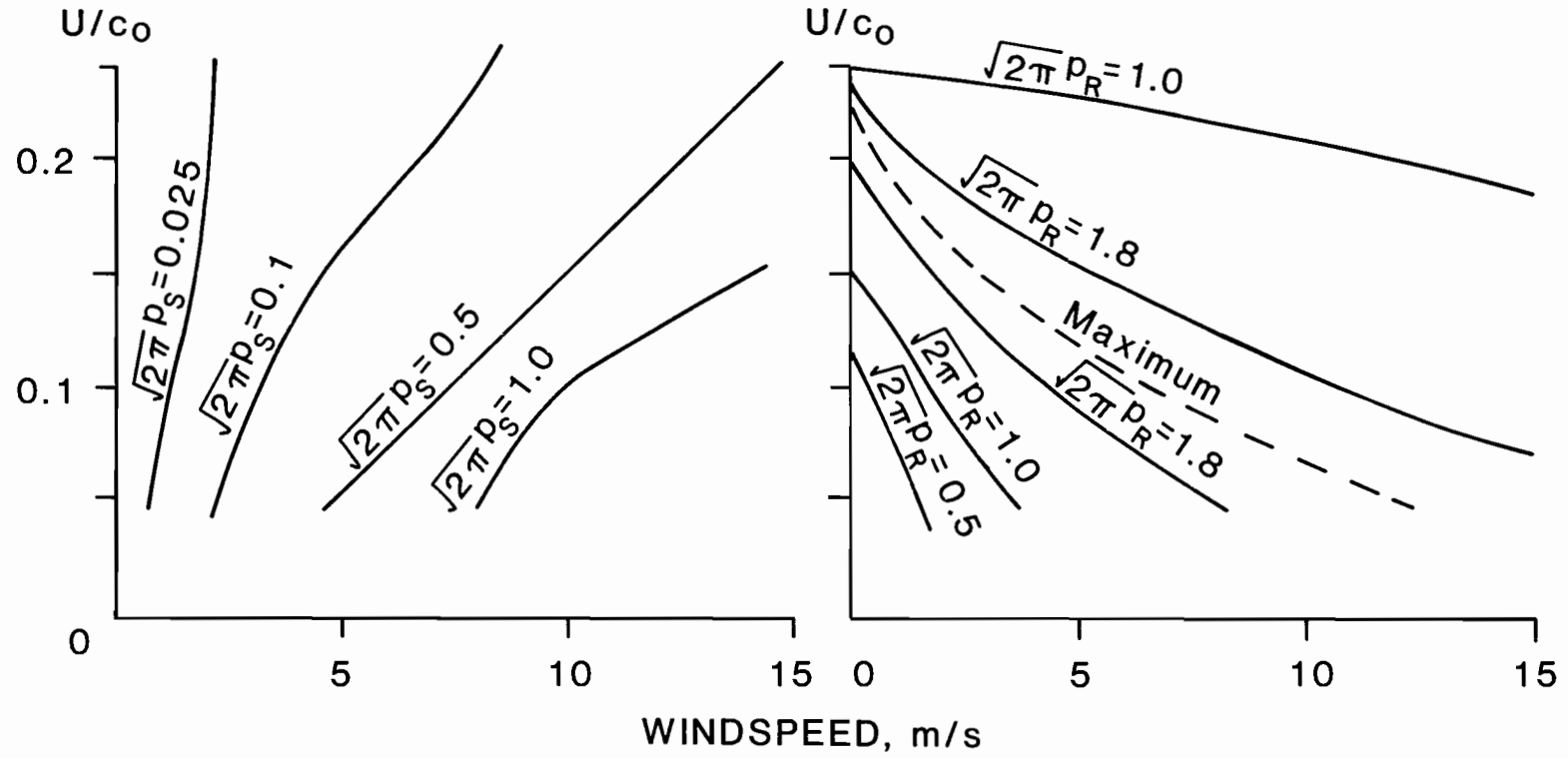

Figure 9 a & b. Isolines of probability of slope 17.5° as a function of windspeed and current speed, showing how P_R decreases with increasing σ_R for large values of σ_R.

increases. As an opposing mean current increases and approaches the critical value of one-fourth the surface-wave velocity, surface waves with velocity 4U (first the shorter, slower ones, then the longer ones) are expected to be strongly amplified and steepened and to break. Whitecaps and foam would then contribute to the brightness of the rough band, which should continue to increase, even though the occurrence frequency of the appropriate slope decreases. If so, the decrease with increasing mean current of the ratio P_R/P_S shown in figures 8 and 9b is unrealistic if the curve is interpreted as contrast.

The unbounded increase of predicted contrast at small values of windspeed (figure 8) is a result of the exponential decrease of the error curve at large values of s_o/σ. In fact, the wings of the slope probability curve merge into a background radiance caused by sunlight scattered in the water, and by reflected skylight (Cox and Munk, 1954). The calculations were repeated with a constant background brightness added to the value of P in (2). These are shown in figure 10, with the same format as figure 8. With this background radiance, contrast caused by current interaction peaks at windspeed 1 to 2 ms^{-1}.

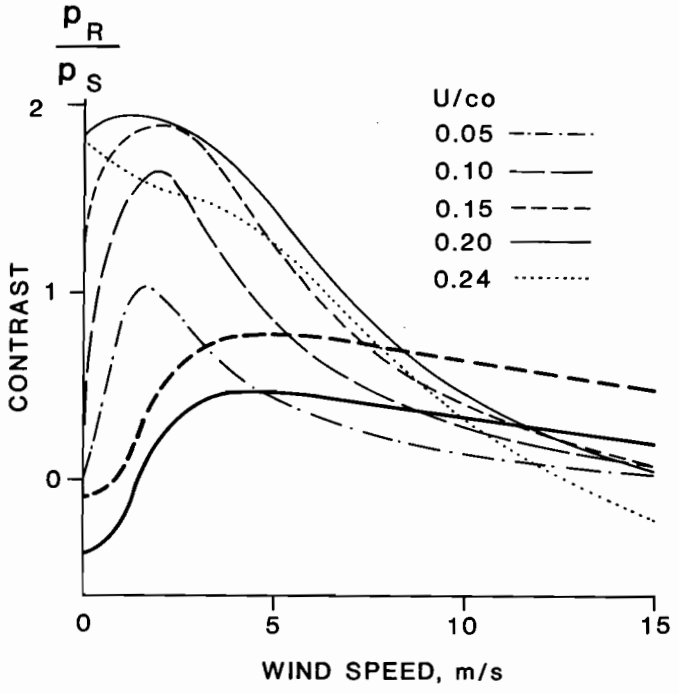

Figure 10. Comparison with figure 8 shows that addition of background radiance to the error function describing the slope probability, P, eliminates the unrealistically high contrast at low windspeed.

The result of the calculation is that the estimated range of observed contrast is matched by values predicted for wave-current interaction for values of the normalized current in the range 0.05 to 0.25 and windspeeds up to 8 m/s. A plausible set of conditions that would fit the range of values of scaled mean current is given by an internal-wave phase speed of 0.5 m/s and amplitude 10 m in water depth of 100 m, so $U \sim \frac{a}{H} c \sim 0.05$ ms^{-1}. Then for U/c_o in the range 0.05 to 0.25, the wavelength of the corresponding surface wave ranges from 0.6 m down to 0.5 mm. The theory, however, is developed for surface gravity waves, not for capillary waves.

B. Oily surface film

The different dependence of mean-squared slope on windspeed in the presence of an artificially produced oil slick, observed and described by Cox and Munk, allows calculation of the contrast between clean and oily surfaces. For each value of windspeed the mean-squared slopes, σ_c and σ_s, are found from (1) for a clean surface and for a slick, and the corresponding values of P are calculated from (2). Then the contrast is the ratio P_c/P_s, shown as the lower full curve in figures 8 and 10. Contrast for an oily slick peaks for windspeed near 4 ms^{-1}, higher than the windspeed at which contrast peaks for wave-current interaction. The fact that bright bands in Landsat images are brighter than the background sea suggests that these bands, assumed in the oily-film hypothesis to overlie divergences in the current system, may occur where the natural oily film is dispersed and the surface rougher than the "clean" surface. To account for this possibility, the lower, dashed curve in each of figures 8 and 10 represent double the contrast of the clean and slick surfaces measured by Cox and Munk. Even this enhanced value barely reaches the lower limit of the estimated range of contrast. These calculations suggest that a natural oily film is unlikely to explain by itself the formation of internal-wave slicks at midlatitudes.

C. Expected variation of contrast with latitude

Figures 11, 12, and 13 show the latitude dependence, as well as the windspeed dependence, of contrast calculated on the basis of the theory of Longuet-Higgins and Stewart. Comparison of one figure to another shows that contrast is decreased when background radiance is increased or when current is decreased. In each case, the latitude dependence is similar, with peak

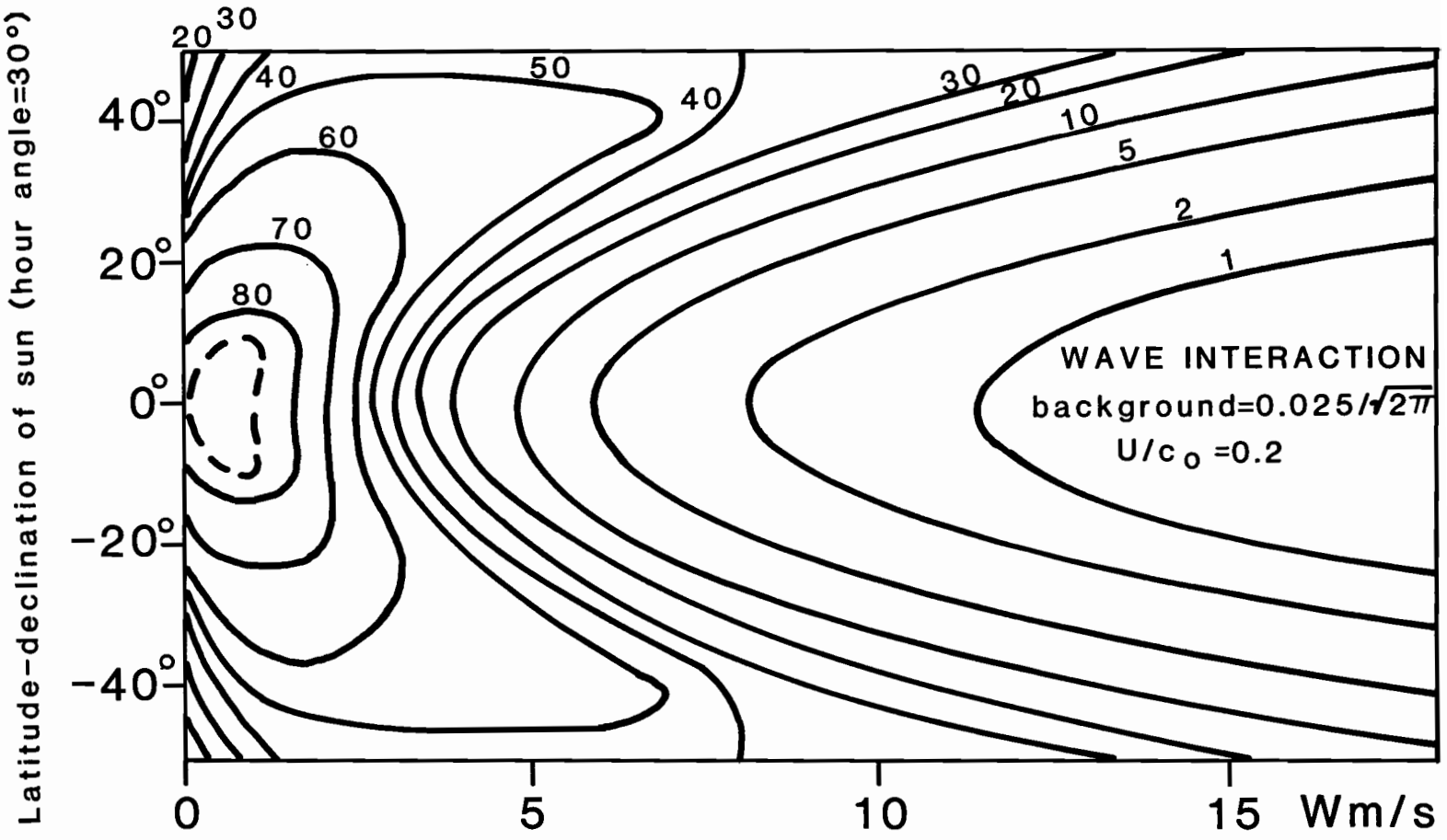

Figure 11. Dependence on windspeed and on latitude of contrast (ratio of radiance of rough and smooth bands) based on Longuet-Higgins and Stewart's theory of surface-wave interaction with current. Contrast is highest for latitude equal to sun declination, at low windspeed.

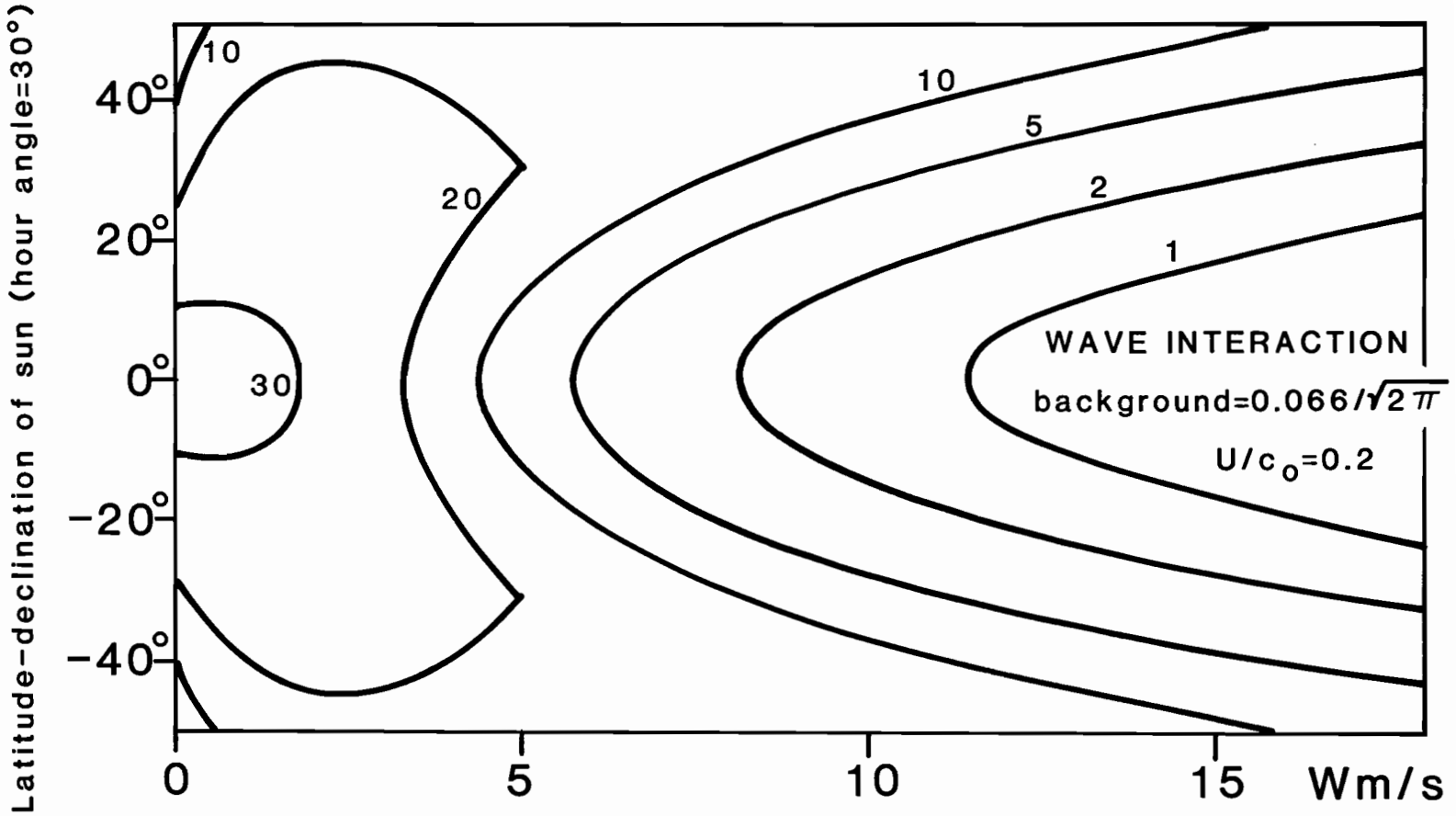

Figure 12. Similar to figure 10, but with higher background radiance. Contrast is lowered, but qualitatively, the dependence on latitude and on windspeed does not change.

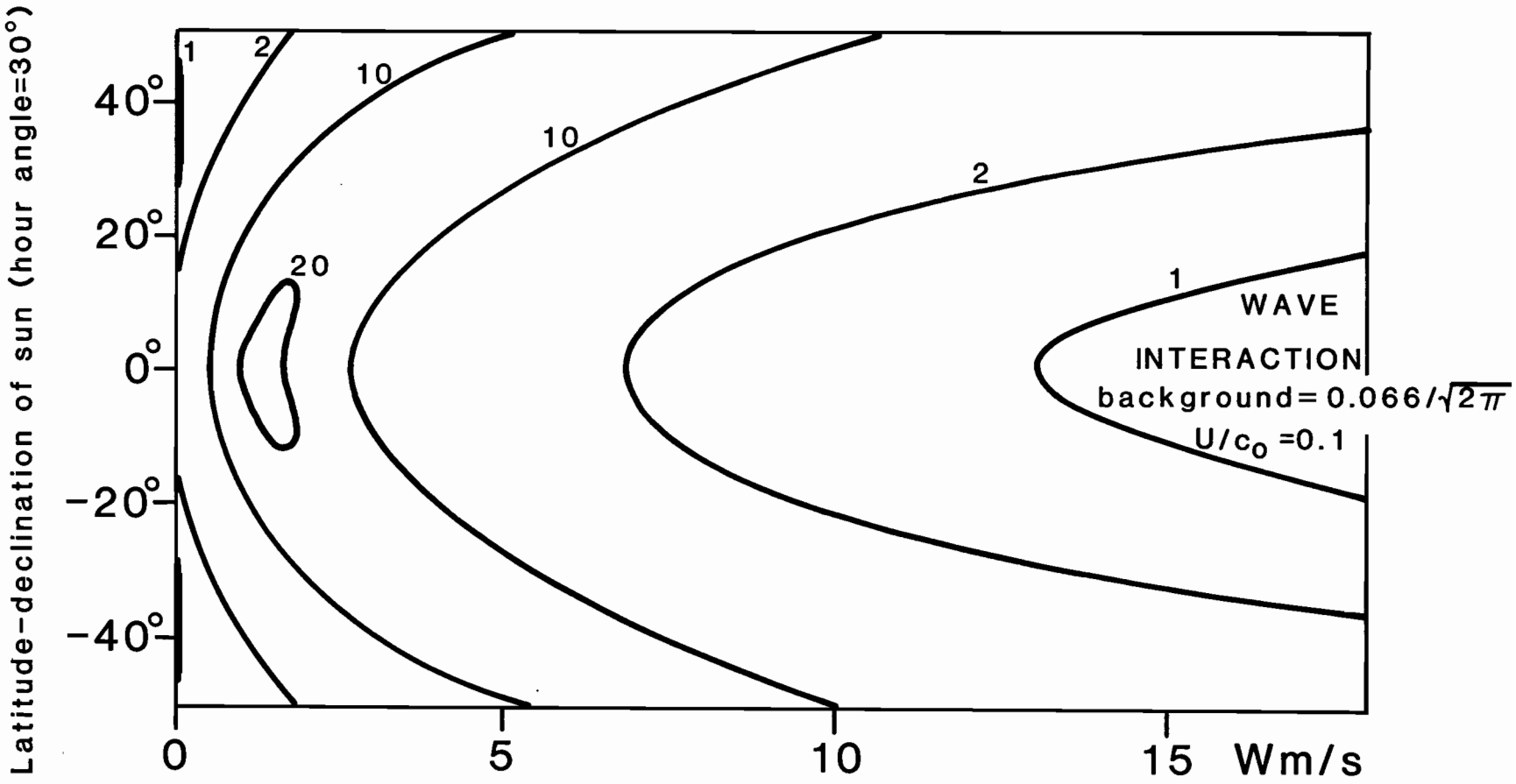

Figure 13. Comparison with figure 11 shows the effect of decreasing the internal-wave current, U, compared to the speed c_o of the undisturbed surface waves. Contrast decreases, and maximum contrast occurs at slightly higher windspeed.

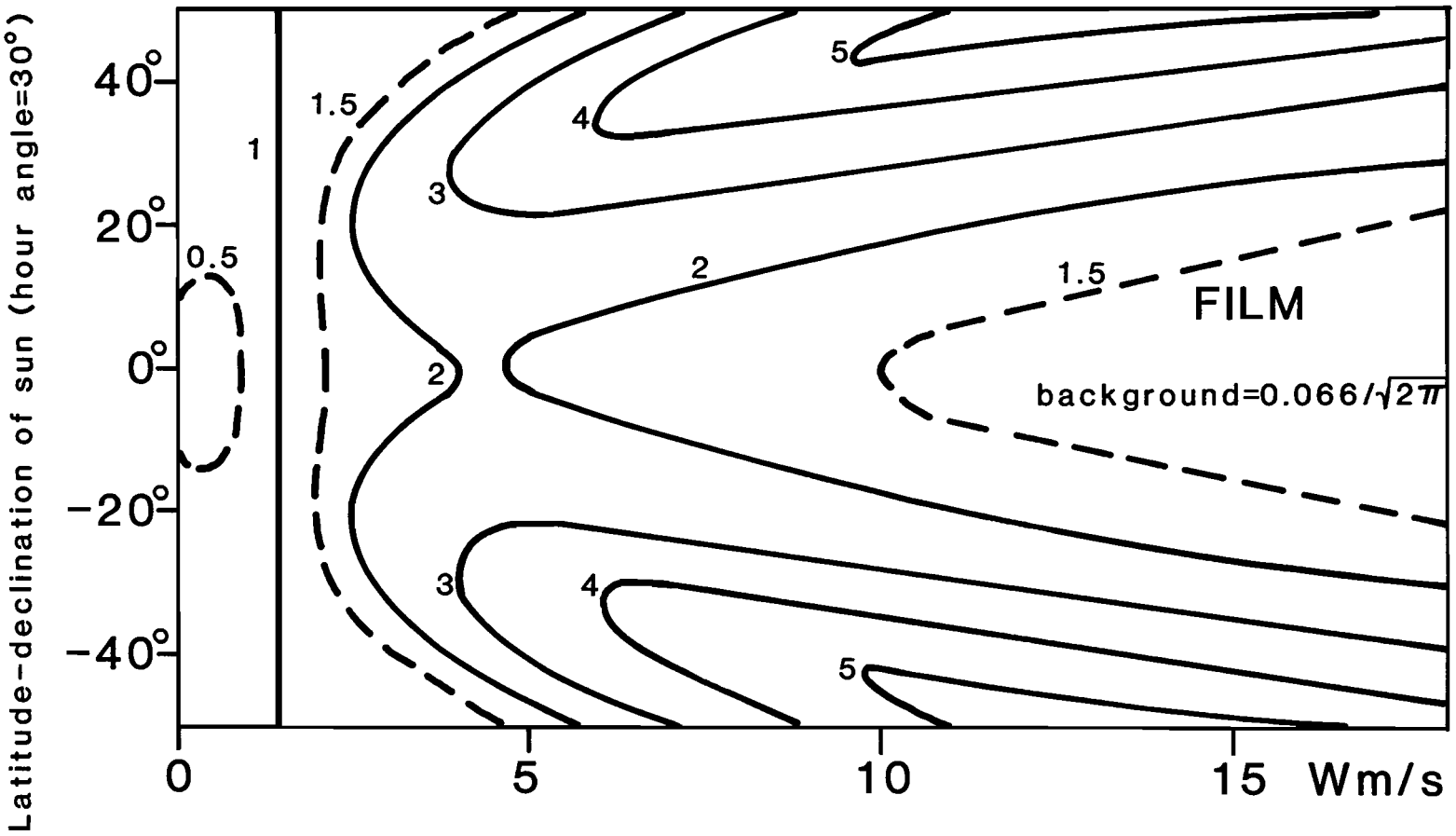

Figure 14. Contours of contrast, similar to figures 10-12, calculated on the basis of Cox and Munk's experimental determination of the effect of an oily film on sea surface radiance. The calculations suggest that this mechanism may be increasingly important, compared to wave-current interaction, at high windspeed, and at high latitude.

contrast at latitude equal to the sun's declination, i.e., for minimum solar zenith distance.

Figure 14 is a similar presentation of calculations based on Cox and Munk's observations of the effect of an oily film on sea surface radiance. Comparison with figure 13 suggests that the film may become increasingly important, relative to wave-current interaction, at high latitudes and at enhanced windspeeds. Moreover, one should note that the calculations for an oily film are based on empirical results, and the calculations for wave-current interaction on theory. Since these calculations were completed, a dynamic theory of wave-current interaction has been developed (Hughes, 1978), and the effect of the internal-wave current field on surface waves has been extensively observed by Hughes and Grant (1978). Their work confirms the significant effect of internal-wave currents on the amplitude and slopes of surface waves, and considerably modifies expectations of the contrast in surface radiance and of the phase, relative to the internal wave, of slicks and rough bands. The experimental results might provide a basis for calculations of contrast that would be more comparable to the film calculations than the theory-based calculations presented here. Finally, one should note that the two mechanisms are not necessarily mutually exclusive.

D. Some other properties of sun glitter.

The curves of figure 10 suggest that to be readily visible, internal-wave slicks require both a moderate windspeed and a sizable surface current as part of the internal-wave velocity field. A surface current with $U/c_o = 0.1$ is sufficient for windspeeds up to about 5 m/s, and stronger currents extend slick visibility to seas roughened by stronger winds, up to 8 or 10 m/s. In a very calm sea (windspeed less than 1 m/s), both rough and dark bands would approach the background radiance and contrast would become low.

Interpretation of sea-surface radiance resulting from glitter leads to expected relations that can be tested with Landsat images. Some of these expectations are that brightness will be less and contrast greater on the western, off-sun side of the image, that the sea will appear brighter when the wind is stronger, and that the image will be darker and show more contrast when the breeze is directed toward the sun from the subsatellite area than when it is oppositely directed.

Brighter sea is expected on the eastern side of the image because the imaged area is west of the center of the sun-glint pattern. A survey of the images published in Sawyer and Apel (1977) qualitatively confirms this prediction, showing that of 19 sets of images, 11 are brighter on the eastern side, 6 show no marked trend in brightness across the image, and only 2 appear brighter on the western side. In making these estimates I attempted to avoid cases where the sea is darker along the coast, which generally lies along the western side of the image. Coastal darkening can be seen in many of the images, for example, in the sets for 1973 July 22, 23, and 24. It extends 70 km ± 40 km offshore and may occur because winds are lighter near land than over the open ocean. Table 1 presents calculated values of the radiance change across the image, and its dependence on windspeed. The mean-squared slope is calculated from $\sigma^2(W) = 0.003 + 0.00512\ W$ m/s and the required slope for reflection is taken as the tangent of 20°.4, 17°.5, and 14°.6 for the western edge, center, and eastern edge of the image. This is appropriate for sun elevation 55°, with sun direction and wind direction both aligned with the scan lines on the image.

The values in Table 1 show that the range of windspeed values from 2 to 15 ms^{-1} corresponds to change in contrast that is comparable to, but less than the change in contrast across the image. Factors that would modify this conclusion are variation in wind direction, consideration of the differences among upwind, downwind, and crosswind slope spectra, changes in sun elevation and azimuth, or a different value of the background brightness, caused by reflection of skylight and by scattering in the water.

To test the expectation that contrast is higher on the darker, western side of the image, sets of images were classified according to the chance of seeing slicks on either side of the image (presence of land and clouds lowers this chance) and whether slicks were observed on either side. Because land lies most often at the western side, the chance of seeing slicks is usually better on the eastern side, and they are indeed observed more often there. More slicks were seen on the eastern side even when the chance of seeing slicks was judged about equal for both sides. However, no slicks were seen on the eastern side when the western side was judged to be more favorable, while slicks were seen on the western side in 4 cases out of 25 when the eastern side was more favorable. The results are summarized in Table 2. In the

absence of any east-to-west change of contrast, and because of land location, one would expect to see more slicks on the eastern side in all but 6 cases out of 47, rather than the 15 exceptions observed. Darker glitter pattern and higher contrast on the western side would explain better-than-expected visibility there, but the difference is less striking than one would expect from the west-to-east contrast enhancement (factor of 15) indicated in Table 1.

Although the across-image and wind-induced brightness changes seem to be in the right range, and the contrast change across the image is qualitatively as expected, there is a paradox in the fact that in most images slicks show enhanced contrast and visibility in bright patches, rather than in the darker, presumably smoother areas. See, for example, the enlarged portions of images for 1973 July 06, 07, and 23, 1974 June 28, and 1974 July 17 of Sawyer and Apel (1977). This behavior would be expected if the sea were rough enough that the root-mean-squared slope exceeded the slope required for glint at the image. The windspeed would need to exceed 35 m/s, 19 m/s, and 8 m/s for this to happen at the western edge, center, and eastern edge of the image; windspeed is unlikely to exceed the first two values in the usual case. The problem requires closer examination, taking into account the direction of the wind and the effect of wave-current interaction on the orientation of surface waves (Gargett and Hughes, 1972), as well as the range of values of sun elevation and of required slope, s_o. The rough calculations and observations presented here suggest that with careful measurements and clear interpretation, Landsat images could provide a good deal of information about the strength, direction, and geographic distribution of winds at the sea surface.

In some cases (July 22 and 23, 1973; June 28 and July 14 and 18, 1974), the leading edge of a packet of internal-wave slicks has the appearance of a front with brighter, supposedly rougher water ahead of the packet, and with the whole packet appearing darker and smoother than the surrounding water. Whether the packet is smoother or the region leading the packet is rougher is not clear from the photographs; this question could probably be answered with study of computer-enhanced images.

Table 1

Slope probabilities and contrasts

Required tilt:		20°.4	17°.5	14°.6	$\frac{Pe + 0.01\sqrt{2\pi}}{Pw + 0.01\sqrt{2\pi}}$
Location on image:		West side	Center	East side	
$\sigma^2(W)$	windspeed				
0.0132	2m/s	0.00844	0.0812	0.667	37
0.0286	5	0.0950	0.415	1.100	11
0.0542	10	0.315	0.685	1.146	3.6
0.0768	15	0.435	0.754	1.08	2.5
$\frac{P_{15} + 0.01\sqrt{2\pi}}{P_2 + 0.01\sqrt{2\pi}}$		24	8.4	1.6	

Table 2

Slick visibility* on eastern and western sides of images

Chance of seeing slicks	East side more favorable	sides equally favorable	West side more favorable	Total
Slicks seen:				
East	21(17)	11(12)	0(3)	32
West	4 (8)	7 (6)	4(1)	15
	25	18	4	47

*Expected number in absence of contrast change is in parentheses.

3. Clouds

The predicted large changes of contrast depending on location on the image and on windspeed lead to the expectation that detection of slicks on Landsat images is sensitive to image location, to windspeed and direction, and

to sun altitude. Image location has been seen to have less effect on slick detection than expected from calculations. A glance at the images (and consideration of missing images) shows that clouds must be the most important factor determining the visibility of slicks. In the following paragraphs an attempt is made to assess the effect of clouds on the slick statistics.

An estimate of cloud cover is published in Landsat data catalogues for each Landsat scene. This estimate seems to pertain to cloud cover over the land in the image, rather than over the ocean or over the image as a whole. This, and the fact that internal-wave packets often are visible through thin clouds, explains the fact that slicks were noted on 13% of the scenes described as having 100% cloud cover. Figure 15 shows that this percentage does indeed decrease as cloud cover increases. From these data, we estimate that of the total of 503 scenes examined, had all clouds been absent, slicks would have been seen on an additional 101 scenes, raising the rate from the observed rate of 30% to the value of 50% observed for cloudless scenes. For this geographic region, where the median value of cloud cover is near 50%, a detector able to work through clouds would need only 60% of Landsat's sensitivity to detect the same number of internal-wave packets.

The question arises whether the identified "packets" may in some cases be atmospheric waves, outlined by clouds. In fact, clouds often show a banded structure of similar scale to that of ocean internal waves. Comparison of clear cases, e.g., clouds over land, and ocean slicks in a cloud-free scene, shows that the internal-wave slicks usually appear sharp edged, because darkened and brightened bands are contiguous. Cloud bands are simply bright bands that typically show soft edges. The statistical behavior of the identified slicks, for example their clustering along the continental shelf, shows that the slick sample cannot be significantly contaminated by cloud bands. To summarize, in spite of the many clouds apparent on the images, slick packets are observed, or partially observed, 60% of the time that they are estimated to be present, and confusion of cloud bands with internal-wave packets appears not to cause significant contamination of the data sample.

4. Seasonal dependence.

Apel et al. (1975a) found internal-wave slicks in the New York Bight area only during summer months, and in this study only images made from May to Sep-

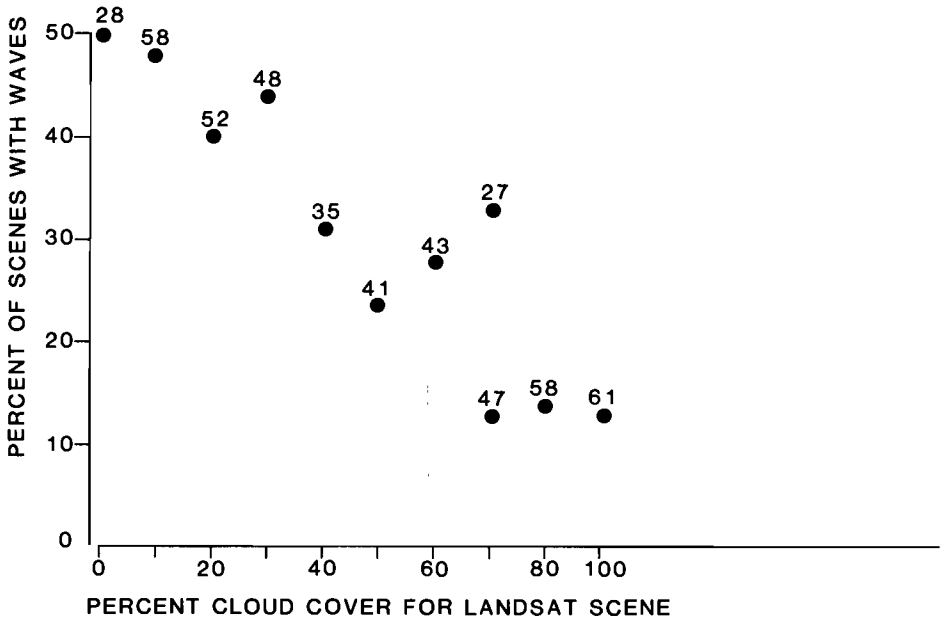

Figure 15. Slick visibility as a function of cloud cover. The numbers over the points refer to the number of images examined.

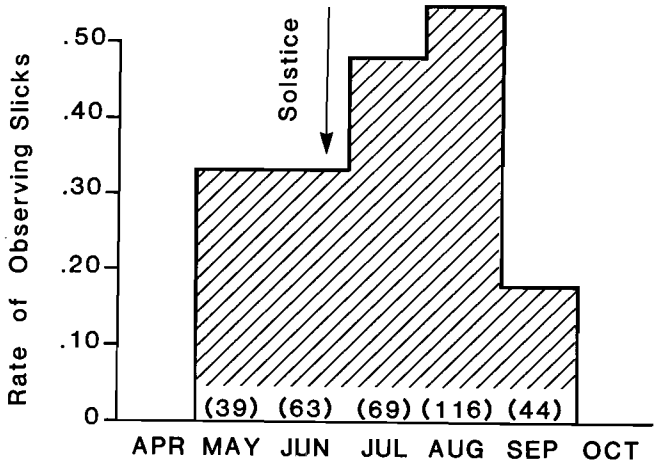

Figure 16. The total number of scenes with cloud cover ≦ 70% is indicated in parentheses, and plotted for each summer month is the ratio:

$$\frac{\text{Number of scenes with slicks}}{\text{Number of scenes with cloud cover} \leqq 70\%}$$

tember were examined systematically. Within this period, the occurrence frequency of scenes with slicks varies by a factor of 3, reaching a peak of 0.55 in August (figure 16). The peak rate occurs, not at the solstice when the sun is nearest the zenith, but late in the summer, when the seasonal thermocline is expected to be most fully developed. August is also the least cloudy month and is clearly the optimum time to go hunting for internal waves in this part of the ocean.

5. Location, occurrence rate, and lifetime of slicks

The close relation of internal-wave slicks to the continental slope is illustrated in figures 17 and 18. The first shows packets from a single set of passes of the satellite and shows clearly how the packets parallel the slope. In the second, the data from three summers, 1972-1974, are superposed; the tendency for lines of packets to parallel the slope can still be discerned.

Figure 20 shows a number of sections across the continental slope; their locations are shown in figure 19. Sections 1, 2, 9, 13, and 14 were chosen because of a relative dearth of internal-wave slicks along the section or its extension. Sections 3, 6, 8, and 10 have slicks over deep water, beyond 200 m. Sections 4, 5a, 5b, 7, 10a, 10b, 11, and 12 have many slicks over the shelf; only 10a and 10b have slicks at the surface of the deep water. Sections 12 through 14 emphasize one point that may explain the dwindling number of slicks going southward from the New York Bight: there simply is insufficient breadth of shelf to hold many packets between the steep slope and the nominally 40-m depth of the mixed layer. A typical profile of Brunt-Väisälä frequency from the 1974 July Nybersex cruise (Proni et al., 1978) in figure 21, shows that the mixed layer extends to about 30-m depth. The maximum density gradient occurs at 45-m depth. Figure 22 shows histograms of values (from Gulfstream, 1975) of the middepth of the first temperature decline for the months of January, March, and April and separately for the summer months, June through September, for the Atlantic coastal region north of Cape Hatteras. In summer the thermocline occurs most often between 30 and 40 m, although there is a group of measurements showing a much deeper thermocline, below 100 m. The deep thermocline is typical in winter. The thermocline-depth histograms illustrate the explanation of Apel et al. (1975a) of the absence of internal-wave slicks in the winter, and confirm that the

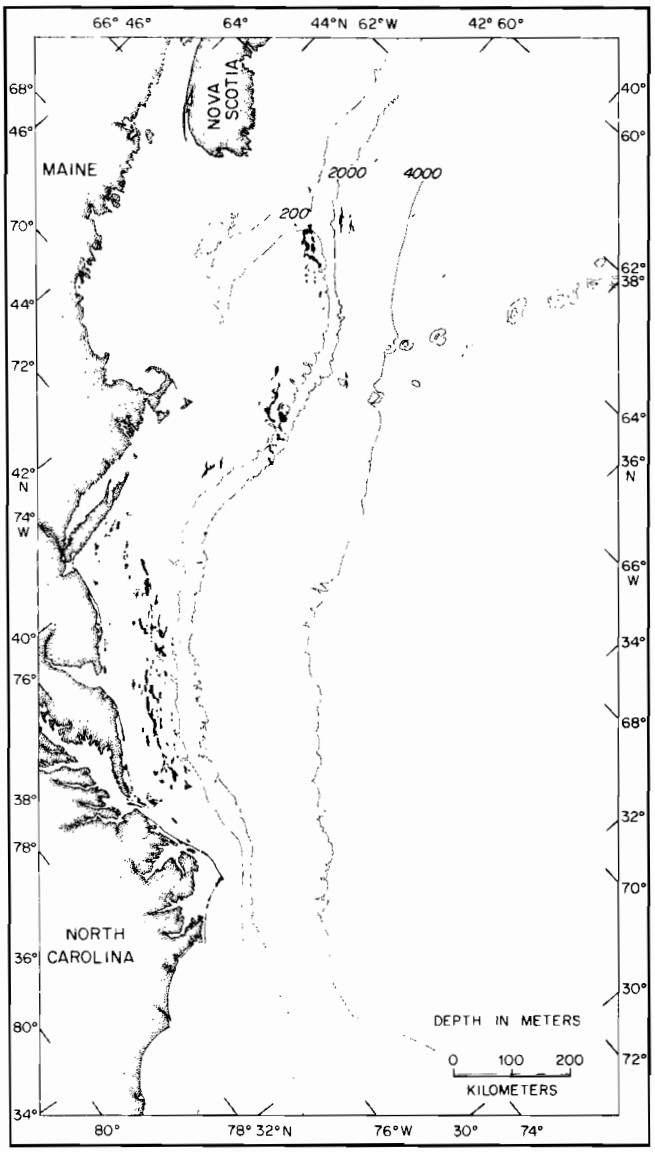

Figure 17. Isobaths for 200 m, 2000 m, and 4000 m are shown, along with superposed tracings of internal-wave slicks for a single set of passes of Landsat I, July 01 to July 07, 1973.

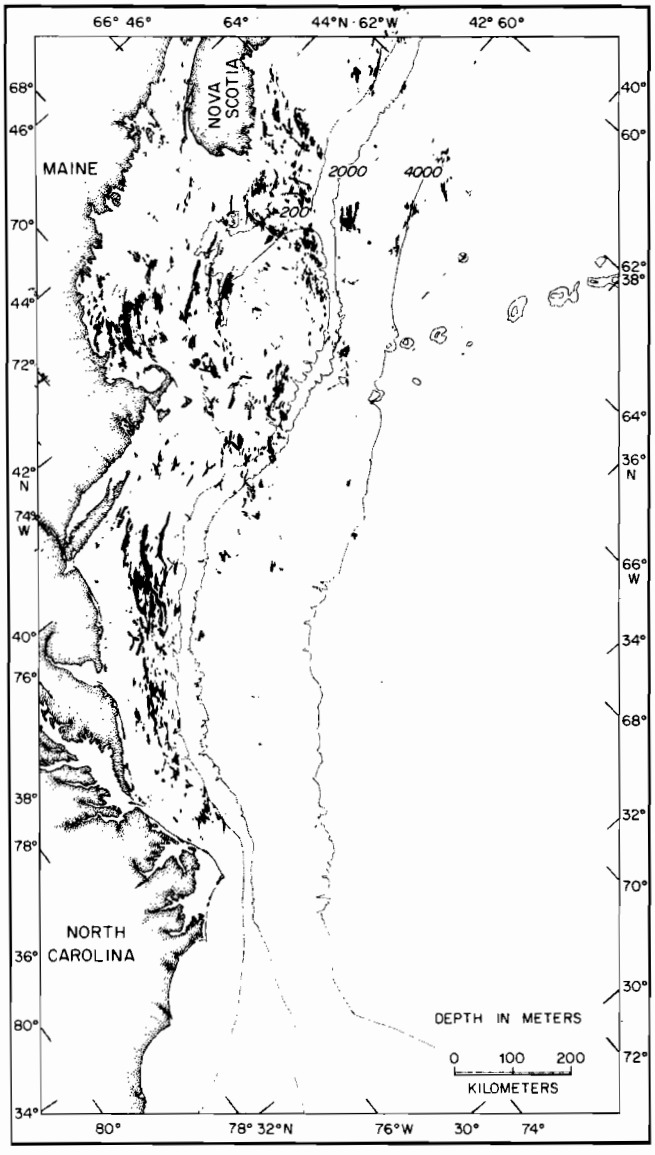

Figure 18. Superposition of tracings of internal-wave slicks, including nearly all the data of the summers of 1972, 1973, and 1974.

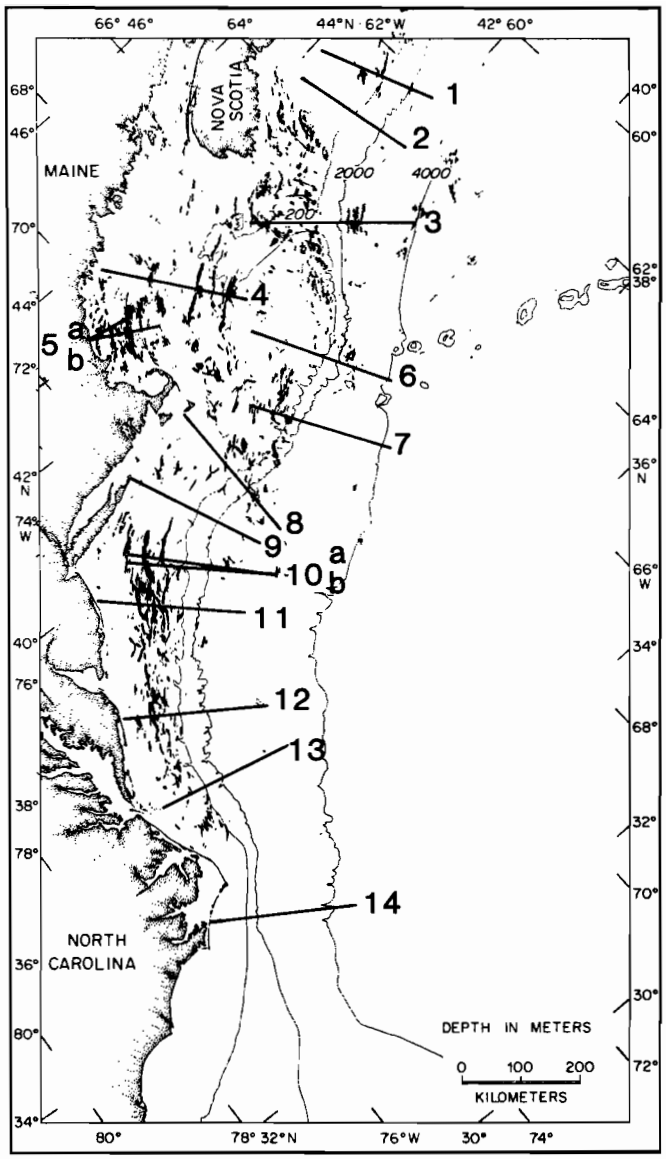

Figure 19. Location of sections shown in figure 20, and of internal waves.

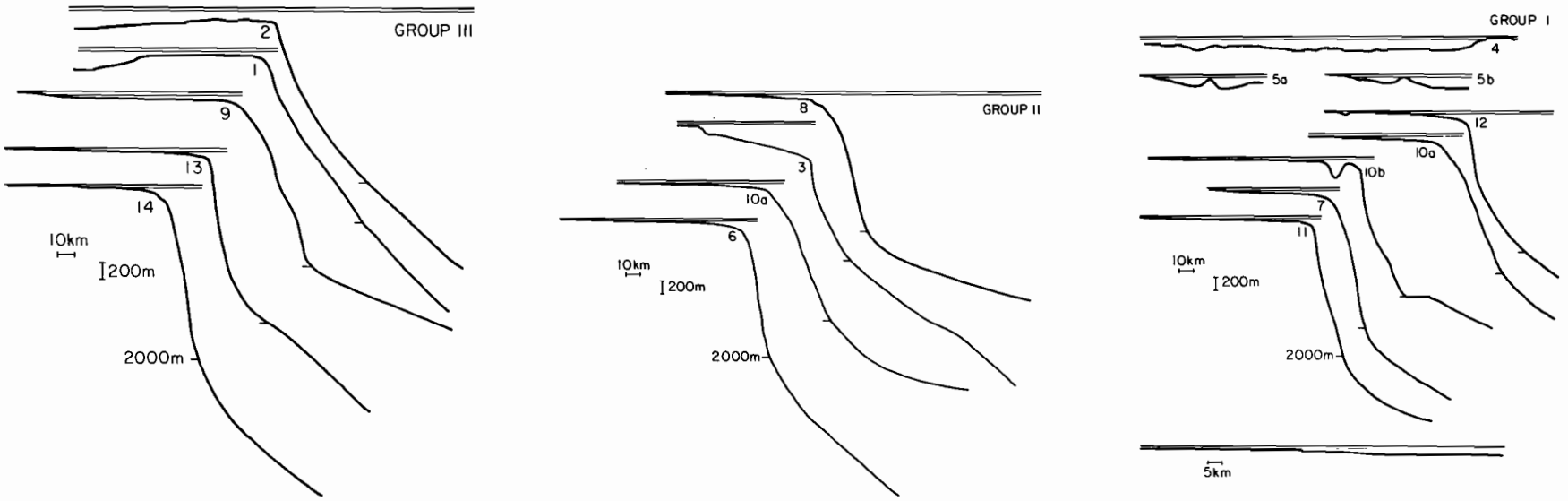

Figure 20a. Sections of continental slope and shelf at locations where there are few internal-wave slicks; b. Profiles for sections that have internal-wave slicks at the surface of deep water, but not (with the exception of profile 10a) many slicks over the shelf; c. profiles for sections that have many internal-wave slicks over the shelf but few or none in deep water, with the exception of 10a and 10b.

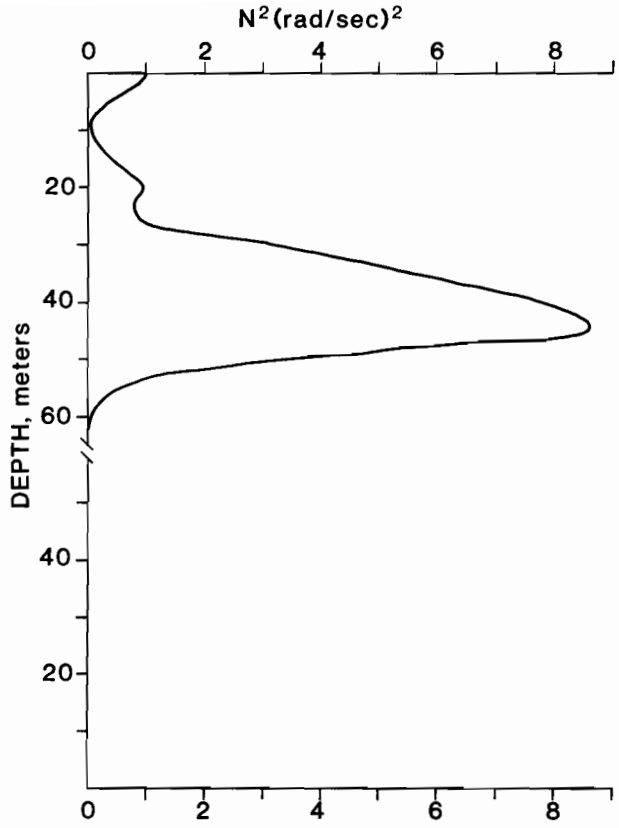

Figure 21. Depth profile of Brunt-Väisälä frequency on the continental shelf in July 1974 (from Proni et al., 1978).

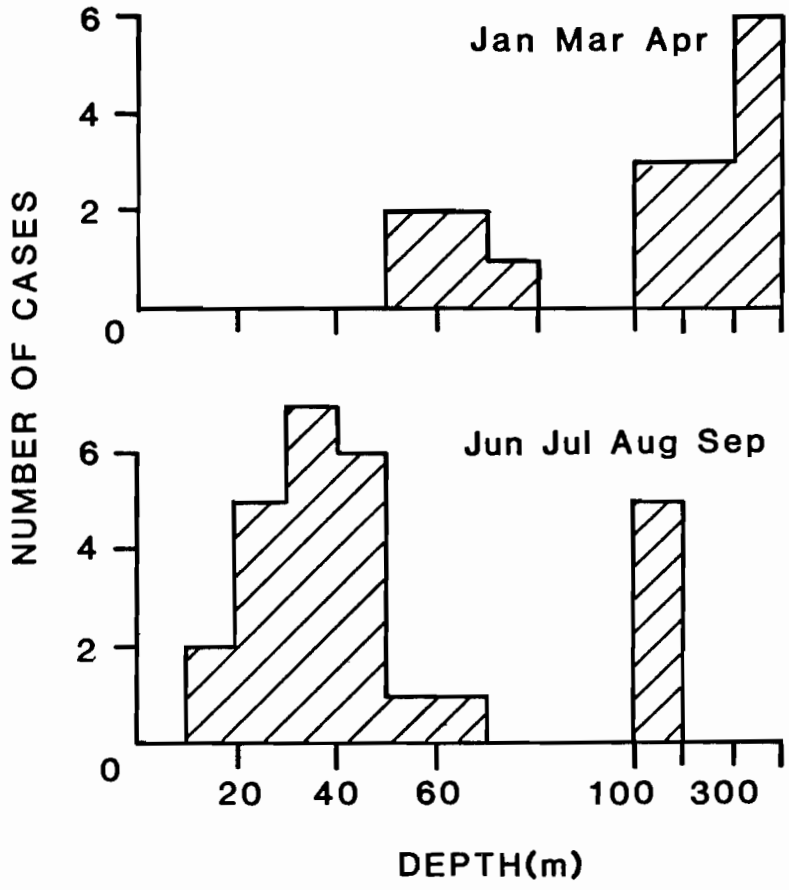

Figure 22. Histograms for winter (above) and for summer of the middepth of the first temperature decline for Atlantic coastal waters in 1975. Data are taken from temperature profiles published in "Gulfstream." Note the nonuniformity of the depth scale.

Nybersex profile is representative for the summer months studied. Figure 23 shows contours that represent the occurrence frequency of slicks, with an attempt to take into account the quantity and quality of data available for the search. The general trends are similar to those conveyed by the composite of slick tracings, indicating that gaps in data or uneven cloudiness do not strongly affect the conclusions drawn from the data.

Another conclusion from the analysis of occurrence frequencies is the non-sensitivity of slick visibility to observing conditions. In some locations, in summer, slicks are seen on nearly every favorable occasion. For example, there are 3 locations where slicks were seen on every image for which cloud cover was no greater than 30%. Evidently slick visibility is not sensitive to sea state or illumination in the range of conditions prevailing near latitude 42°N in the summer months at the time of the satellite passes (2 or 3 hours before noon).

Another factor in the southward decline of slick occurrence frequency may be the weakening of rotary tidal currents (figure 24). A puzzle, and possible clue, is the fact that the shelf from Delaware Bay to Cape Hatteras shows many slicks in July 1973, but few in 1972 and none in 1974.

A possible association of deep-water internal waves with canyons is described by Shepard et al. (1974). However, the slicks on the eastern continental shelf do not show a strong association with canyons, with the exception of Northeast channel and possibly Hudson Canyon (figure 18).

Figures 25a and b show that the peak frequency of slick occurrence is centered at 80-m depth. The number of slicks drops sharply for water shallower than 40 m as expected if the pycnocline is near 40-m depth. A glance at the charts in Sawyer and Apel (1977) showing slicks superposed on bathymetry confirms that almost no slicks occur shoreward of the 40-m depth contour. On the deep-water side of the histogram peak, occurrence frequency drops rapidly, then levels off. The counts at depths beyond 200 m are detailed in Figure 25b, which shows a small secondary peak for depths between 2000 and 3000 m. This secondary peak is evidently a consequence of the fact that there is little water surface overlying the steep slope at depths 200 to 2000 m. When the counts in each depth interval are divided by the (roughly) estimated surface area of water at that range of depths, the normalized counts decrease smoothly and exponentially, as shown in figure 26. In the vicinity of the continental slope, at locations where internal-wave slicks are observed at the

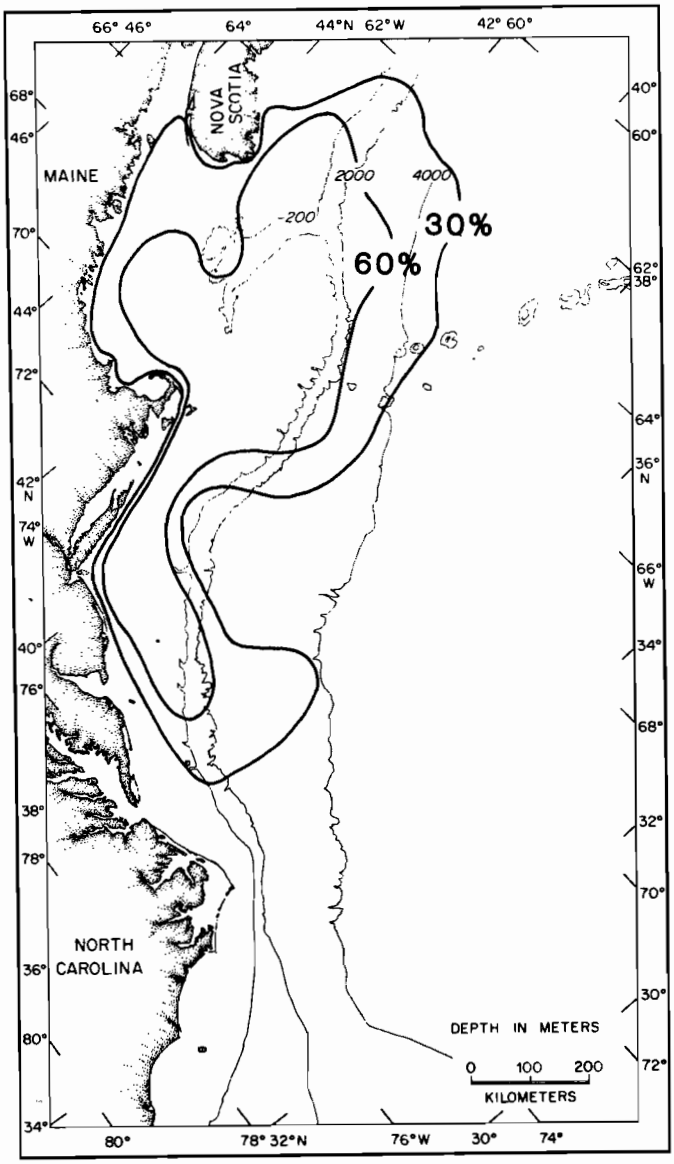

Figure 23. The frequency of observation of slicks at each geographic location has been roughly normalized according to the number of available images and the percentage of cloud cover to derive these contours of occurrence frequency.

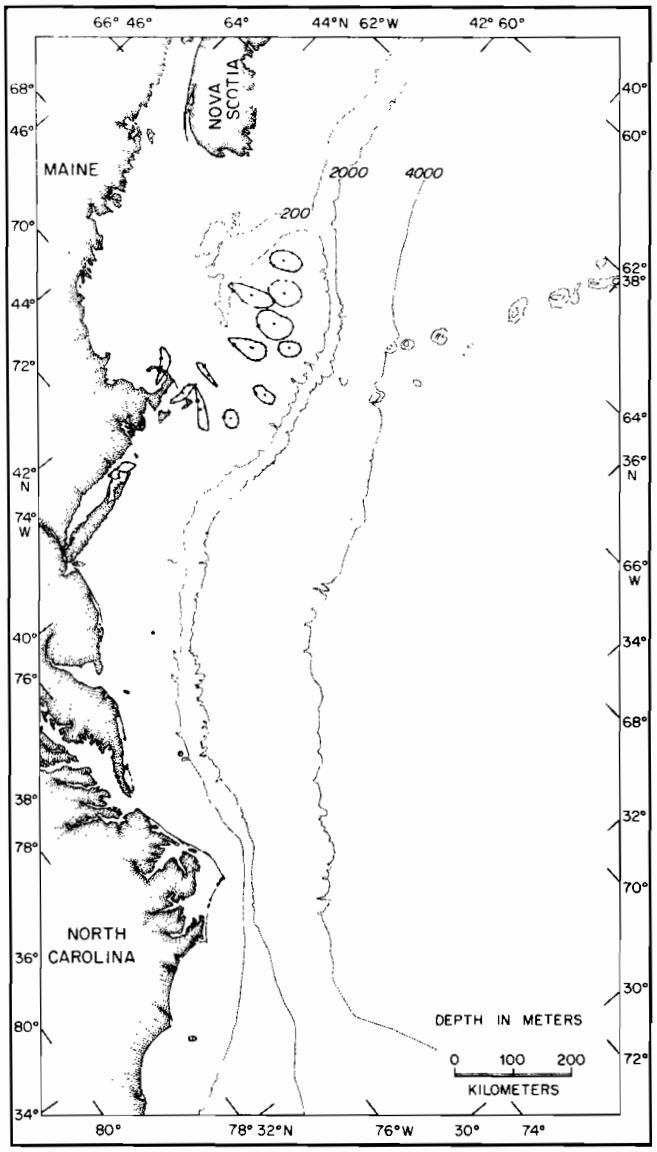

Figure 24. Rotary tidal currents in the region studied. Polar diagrams represent the strength and direction of offshore rotary tidal currents. The large dot marks the phase of flood tide at Pollock Rip Channel. The strongest current is 2.4 knots (1.2 ms^{-1}).

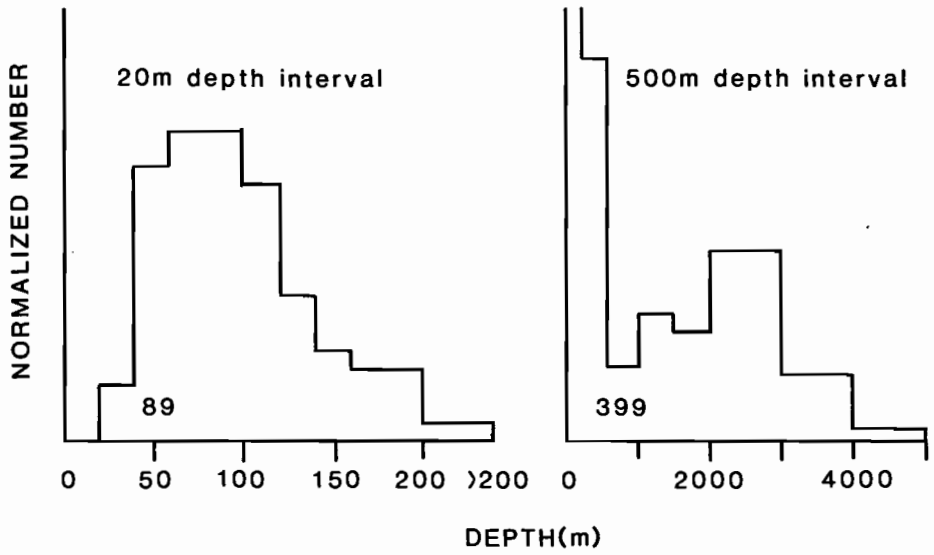

Figure 25. Histograms of the water depth where slicks are observed. The counts of slicks are normalized for depth interval, but not for surface area at each depth. (a) depths <200 m (b) depths >200 m.

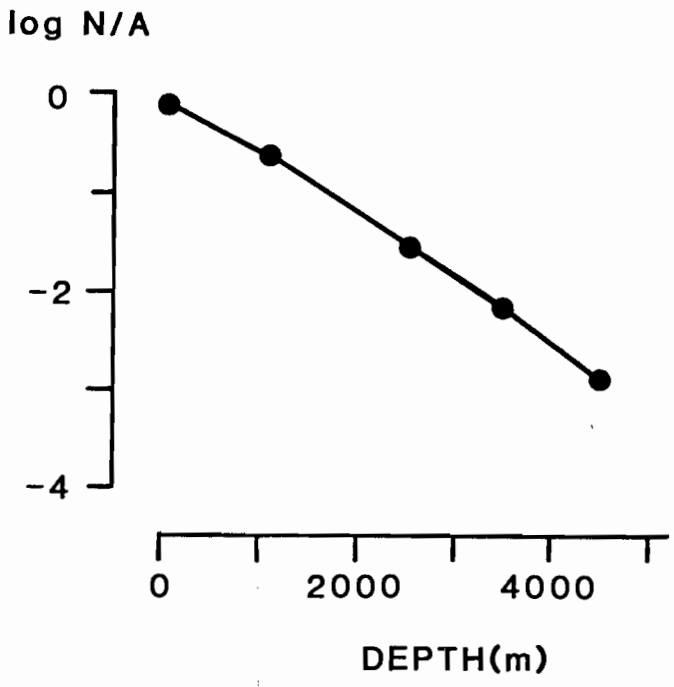

Figure 26. The slick counts in each interval have been normalized for surface area. The plotted value is the probability of observing a surface slick in water of a given depth.

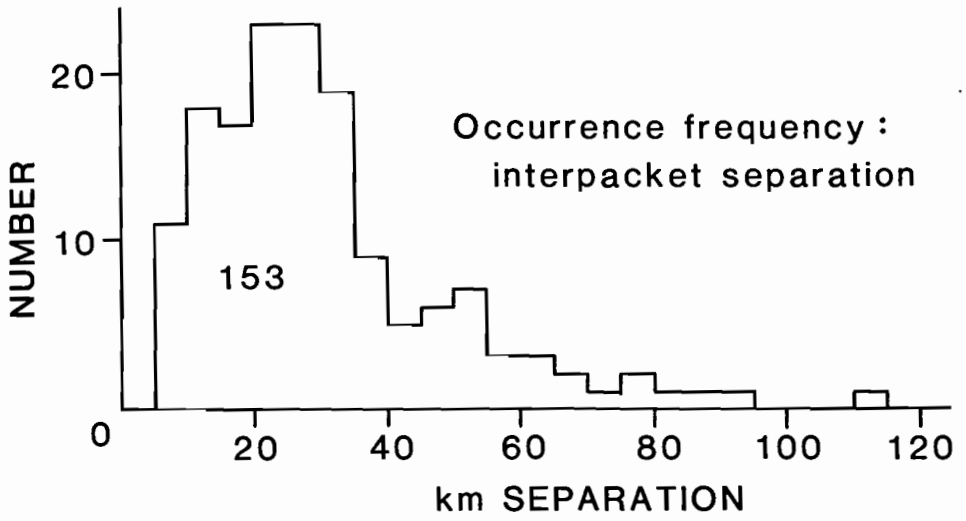

Figure 27. Number of packet pairs as a function of packet separation in kilometers.

surface, the depth distribution peaks where the depth is about twice the depth of the pycnocline, going to zero where the depth equals the pycnocline depth and the subpycnocline layer disappears, and decreasing exponentially toward greater depths, so that occurrence frequency has dropped by a factor of 10^{-3} where depth is 100 times the pycnocline depth.

Apel et al. (1975a) noted that similar packets often are separated by a distance that corresponds to a propagation speed of about 0.5 ms^{-1}, given the tidal period of 12.5 h. Figure 27 shows the frequency of occurrence of distance of separation in 153 packet pairs. In most cases these pairs or series of packets are seen on a single image, as in figure 1. These are interpreted as packets generated at the same topographic feature on successive tides. Some are packets seen at nearly the same location on overlapping portions of images made on successive days; these are thought to have been generated at the same place two tidal cycles apart (July 23, 24, 1973; August 6, 7, 8, 9, and 10, 1973; August 22, 23, 1974). In other cases, packets are seen on images made on successive days. The packet on the later image lies shoreward of the packet in the earlier image and can be identified as the same packet, two cycles later. In some cases the intervening packet is present, in some cases it could be obscured by clouds or off the image (August 10, 11, 1972; July 22, 23, 1973). The peak in occurrence frequency of interpacket separation between 20 and 30 km is echoed at 50 km and faintly at 75 km. The data are consistent with a typical separation of 25 km. The long-wave approximation to the group and phase velocities is

$$c_o^2 = g\Delta\rho \frac{h_1 h_2}{h_1 + h_2} \tag{7}$$

where h_1 and h_2 are depths of the lower and upper layers, $\Delta\rho$ is the density difference between layers and g is gravitational acceleration. With $h_1 = h_2 = 40$ m, a value of 0.0017 for $\Delta\rho$ fits the deduced velocity. With the same upper-layer density and depth, and total depth 3000 m, the velocity would increase to correspond to a packet separation of 35 km.

If the packets are generated where the slope reaches approximately 200-m depth (figure 18), the distance of a packet from the slope should be a measure of its age: packets generated within one-half tidal cycle of the time of the image should be within 12.5 km of the 200-m contour, those generated from 0.5 to 1.5 cycles earlier should be between 12.5 and 37.5 km from the contour,

and so on. Figure 28 shows the distribution of deduced ages of the packets appearing in figure 27. After one day, the number of packets decreases with distance from the slope, falling below 20% by the fourth day. The "half life" of a packet (time for half the packets to disappear) lies between the second and third tidal cycle for packets on the shelf. The sparse data for packets in deep water show a distribution of slope distance consistent with this value of half life. They are treated in the same way as the on-shelf data, scaling the distance from the 200-m contour by 35 km, the typical distance traveled during the tidal cycle in water of 3000-m depth.

The data for off-shelf packets are plotted as crosses in figure 28. The number of recognized packet pairs in figure 27 falls off faster with increasing separation than do the relative numbers in figure 28. There are 46 pairs with separation of 20 to 30 km, 21 pairs with separation between 40 and 60 km, and 11 pairs with separation 60 to 90 km, so the relative number has fallen off to 0.46 by the second cycle and 0.24 by the third, compared to 0.70 and 0.30 derived from the distances of packets from the shelf. The recognized series of packets (figure 27) may be subject to more interference from clouds.

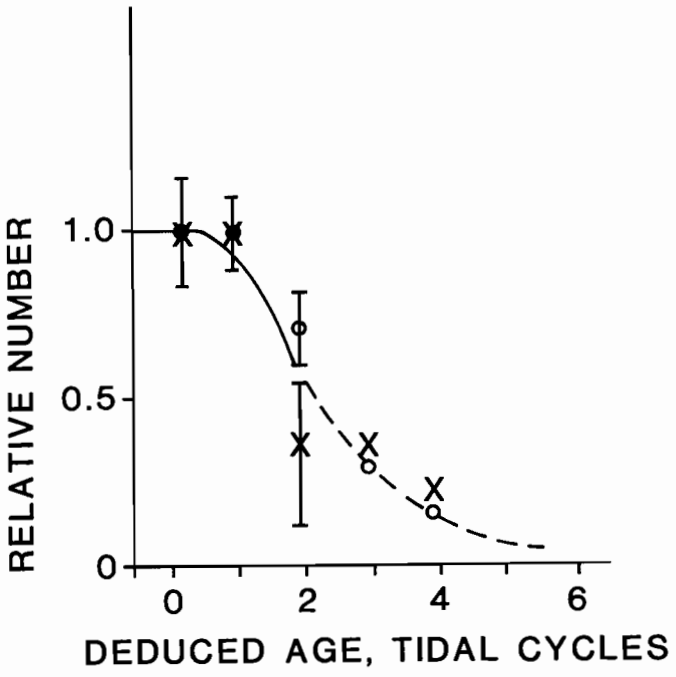

Figure 28. Fraction of surviving packets as a function of distance from the continental slope. Distance is scaled by the distance traveled in one tidal cycle, 25 km on the shelf, and 35 km in deep water, so that it can be interpreted as age.

In any case, the conclusion can be drawn that nearly all packets survive past one tidal cycle, and that about 25% of the packets survive for at least 3 tidal cycles.

The deduced long life of internal-wave packets on the continental shelf is an unexpected result and invites further examination. The satellite images are snapshots and do not provide the continuity required to demonstrate unquestionably the uninterrupted existence of any one packet. The existence of series of packets, and of packets that can be identified on successive days, are reasons for believing that the packets often last for two or more tidal cycles. Another is the evidence that they are generated at a steep slope, along with the fact that they are found at distances from the slope corresponding to travel times up to four tidal cycles. On the Nybersex cruise (Proni et al., 1978), R/V *Westward* passed repeatedly through an internal-wave packet during an interval of two hours, providing direct evidence of continuous existence of the packet over at least this interval of time. In section 10, a lifetime longer than an hour is shown to require significant nonlinearity in the wave equation.

6. Wavelength spectrum, number of slicks in packet, packet extent

The spectra of wavelengths measured within 115 packets on the continental shelf and 9 deep-water packets are shown in figure 29. The peak between 400 m and 500 m for waves on the shelf is well above the limiting resolution of about 80 m for Landsat images, indicating that the rapid drop in frequency of occurrence for short waves is real rather than imposed by the conditions of observation. The decrease on the long-wavelength side of the distribution is more gradual, and the distribution's median value of 600 m is well above its peak value. In deep water (~3000 m), wavelengths tend to be longer, and the spectrum is much flatter; the peak is at 750 m and the median value at 850 m. In these 115 packets for which wavelengths were measured, the average number of slicks is 7, but in a somewhat larger sample of 151 packets that includes these plus other packets for which only the mean wavelength was measured, the most likely number of slicks is about 5 (figure 30). We conclude that the wavelength spectrum of internal waves on the continental shelf is not smooth and exponentially decaying, like the Garrett-Munk (1975) spectrum that fits so many observations of internal waves in the open ocean. The spectrum of these near-source waves has two well-separated peaks, one at wavelength 26 km,

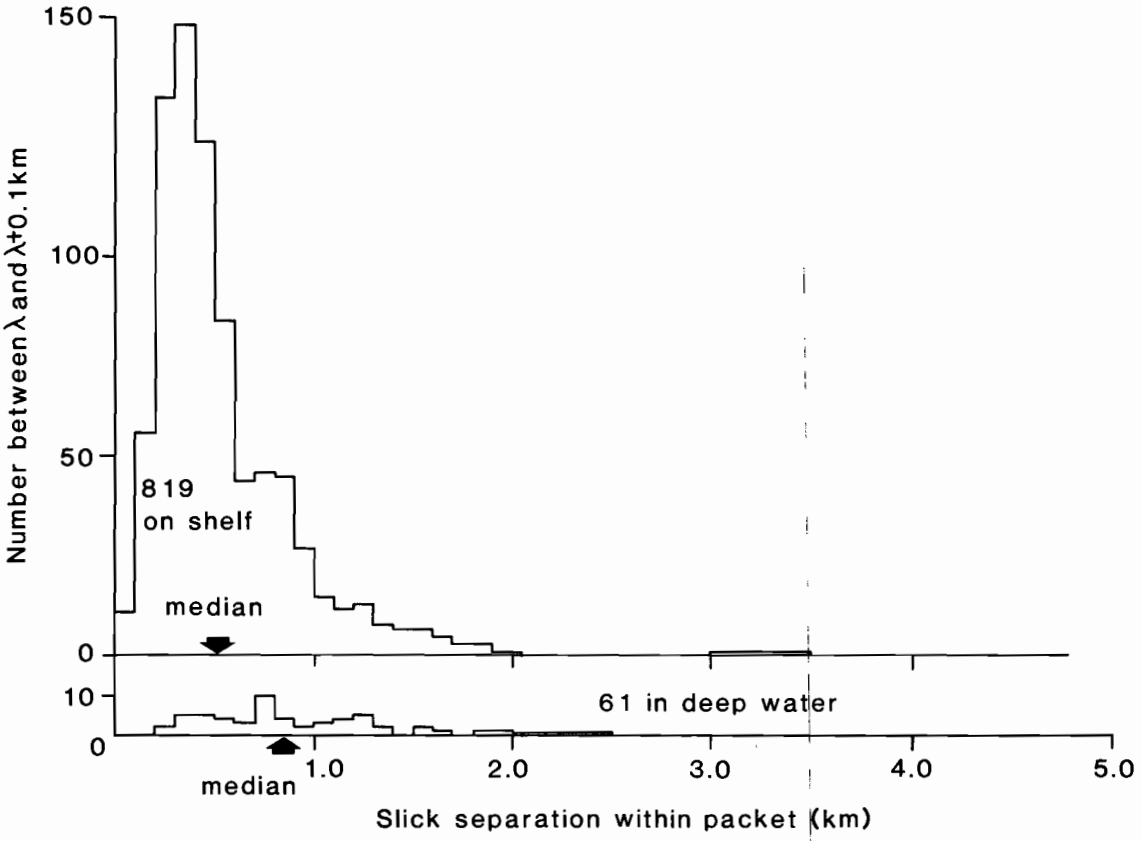

Figure 29. Distribution of values of slick separation in internal-wave packets on the continental shelf.

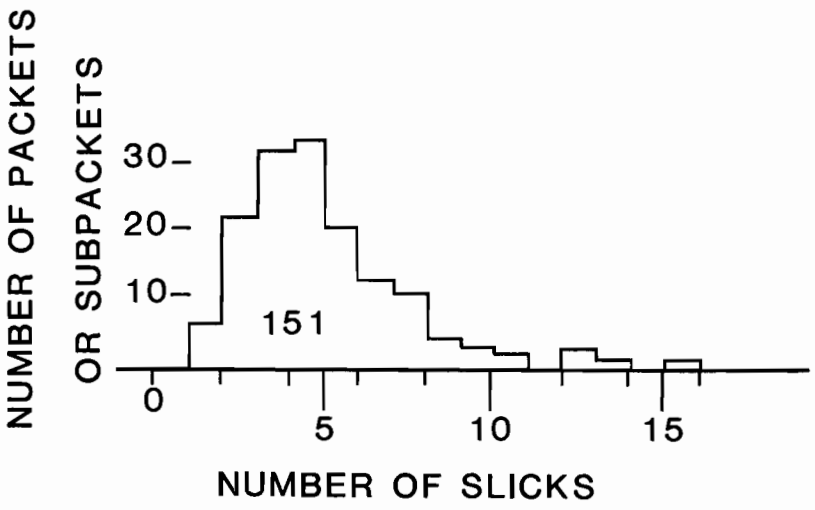

Figure 30. Histogram of number of slicks within packets or subpackets.

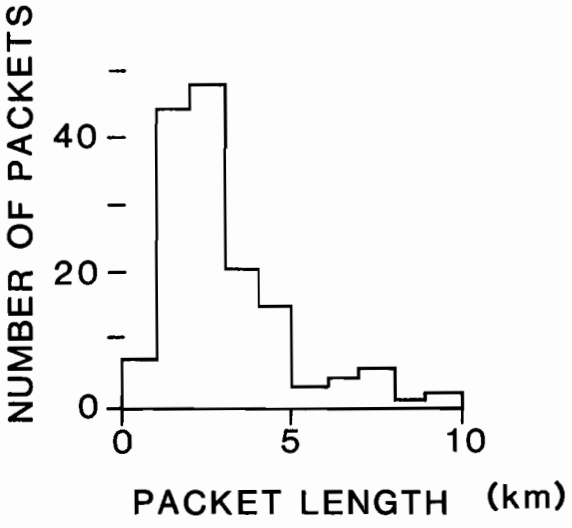

Figure 31. Distribution of values of front-to-rear length of packets on the continental shelf.

which can be identified with the tidal cycle, and the other near 450 m, which is several times the depth of the water where most of the waves are found. Apparently the wave spectrum preserves evidence of the circumstances of its generation over time spans of several wave periods and over distances of several wavelengths.

The front-to-back extent of packets varies in the range 1 to 10 km, with the most likely value 3 km, as shown in figure 31.

7. Radius of curvature

A polar grid on transparent material permitted measurement of the radius of curvature of the slicks in internal-wave packets. The frequency distribution for 94 packets is shown in figure 32. The distribution peaks between 20

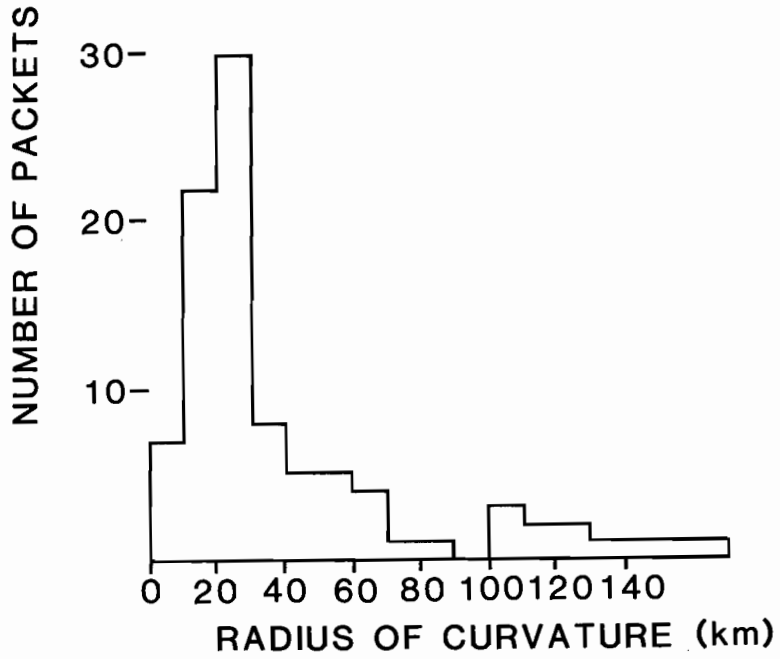

Figure 32. Occurrence frequency of radius of curvature for 94 internal-wave packets.

and 30 km, as does the distribution of values of interpacket separation (figure 27), but large values of radius of curvature occur more frequently than large values of interpacket separation. The radius of curvature was measured with the idea that the wave source might lie at the center of curvature. In fact, the shape of the waves is expected to be and appears to be sensitive to topography, so that the center of curvature is at the source only very early in the life of the wave. In the whole data sample, radius of curvature bears no consistent strong relation to wavelength, to water depth, or to other characteristics of the packet.

8. Wavelength dependence on depth and season

The long-wave approximation to the wave speed (7) implies that the squared wave speed varies as $\Delta\rho\ h_1\ h_2/H$, so that in water deep enough that the ratio of lower-layer depth to total depth, h_1/H, changes little, c^2 varies as $h_2\ \Delta\rho$, or as the product of depth with density defect of the upper layer. Möllo-Christensen and Mascarenhas (1979) have used this relation, along with measured values of the separation of internal-wave packets, to estimate the heat content of the upper layer, assuming that the density change results from temperature change alone. Their comparison with shipboard observations shows the estimate based on wave speed to be lower than the shipboard measurements by a factor of 0.6. Several factors could be included in the calculation that would raise the value of the satellite-based estimate. With

$$c^2 = g\Delta\rho\ \frac{h_1 h_2}{H}\ , \tag{7}$$

and with stored heat in the upper layer:

$$Q = \rho_1\ C_p\ \Delta T\ h_2, \tag{8}$$

and

$$\Delta\rho = \alpha\rho_2\ \ \Delta T$$

(neglecting density change resulting from salinity change)

$$Q = \frac{\rho_1}{\rho_2}\ \frac{C_p}{\alpha}\ \ \Delta\rho\ h_2$$

$$= \frac{\rho_1}{\rho_2}\ \ \frac{H}{h_1}\ \ \frac{C_p}{\alpha}\ \ \frac{c^2}{g}\ . \tag{9}$$

Möllo-Christensen and Mascarenhas take c corresponding to an interpacket separation of 12 km, and take the depth of the upper layer as 10 m; we have found the fundamental interpacket separation to be 26 km, and the upper-layer depth to be 40 m. Their values lead to wave speed of 0.27 m/s and $\Delta\rho = 0.0008$, while for ours the corresponding quantities are 0.58 m/s and 0.0014. The possible revisions of their estimate of Q are these:

(1) double the value of the wave speed, interpreting the histogram of figure 22 as indicating a basic intertidal wavelength of 26 km. This increases the estimated value of Q by a factor of 4.

(2) interpret the interpacket distance as related to a group speed. The phase speed in expressions (7) and (9) then can be greater than the group speed and Q can increase. The assumed equivalence of group and phase speed is consistent with use of the long-wave limit for c^2, but this latter approximation also tends toward underestimation of Q: $c_o > c > c_g = \frac{\text{separation}}{\text{period}}$, and Q again would increase.

(3) include the factor H/h_1, which is always greater than one, and so h_1 increases the estimated value of Q.

Möllo-Christensen's and Mascarenhas's satellite-derived estimate of heat content seems likely to be too small, by even a greater amount than indicated by their comparison with direct ocean measurements.

The data in this study show a seasonal trend that agrees with the effect discovered by Möllo-Christensen and Mascarenhas. Table 3 displays the mean value of the interpacket separation for a small sample of packets for which various characteristics of the packet have been measured. The sample is divided according to the season when the packets were observed. This small sample indicates a steady increase of wave speed through the season, resulting in a change of the square of the wave speed, which measures heat content of the upper layer, by a factor greater than 5. The variances given in the table are for the mean values. They indicate that even a small sample of measurements of separation provide a precision that is meaningful in terms of the seasonal trend.

Table 4 shows a possible schedule of summer warming and deepening of the upper layer that would match the increase in wave speed found in Table 3.

Another property of wave packets, the wavelength of the shortest waves in the packet, appears to measure the depth of the upper layer, while the wavelength of the longest waves in the packet depends on the total depth. Tables 5 to 8 are contingency tables for wavelength and season, and for wavelength and depth. The tabulated quantity is the observed number of cases, follwed by the expected number, in parentheses. χ^2 is estimated as the sum of the quantities: (observed number - expected number)^2/expected number. The tables show that the wavelength of the shortest waves in the packet increases significantly as the season advances, while its dependence on total depth is not significant. The longest wavelength, on the other hand, depends significantly on depth, but not on season. A quantity that increases as season advances and that could influence wavelength is the depth of the upper layer, and it seems reasonable to take as a working hypothesis that the shortest wavelength in the packet is determined by the depth of the upper layer. Table 9 shows that the depth of the water where packets are observed does not change significantly with season. The weak tendency for more packets to be observed in deep water early in the season tends to oppose and weaken the significant relations; this shows that they are not determined accidentally by such a trend.

Of the longest waves, the group in shallow water, with mean depth 70 m, has mean wavelength 760 m, while the group in relatively deep water of mean

Table 3

Season	Mean interpacket separation, km	No. pairs in sample	Normalized separation	Relative c^2
June	13.5 ± 2.5	2	1.0	1.0
July, 1st half	19.4 ± 1.3	5	1.44	2.07
July, 2nd half	29.4 ± 2.7	5	2.19	4.78
August	30.9 ± 4.8	8	2.29	5.24

Table 4

Month	bottom temp.	upper-layer temperature	S = 35°/°° $\Delta\rho$	h_2,m	h_1,m	c_o ms^{-1}
June	8°	15°	0.0013	16	84	0.41
August	8°	25°	0.0038	40	60	0.94

Table 5

Wavelength of shortest waves:	≦ 300 m	> 300 m	
Season:			
before mid-July	19 (13)	18 (24)	37
after mid-July	16 (22)	46 (40)	62
	35	64	99

$\chi^2 = 6.8$, $P(\chi^2) \sim 0.01$

Table 6

Wavelength of longest waves:	≦ 800 m	> 800 m	
Season:			
before mid-July	23 (21)	14 (16)	37
after mid-July	33 (35)	29 (27)	62
	56	43	99

$\chi^2 = 0.70$ $0.25 < P(\chi^2) < 0.5$

Table 7

Wavelength of shortest waves:	≦ 300 m	> 300 m	
Depth:			
< 100 m	32 (29)	32 (35)	64
100 to 200 m	13 (16)	22 (19)	35
	45	54	99

$\chi^2 = 1.6,\ 0.1 < P(\chi^2) < 0.25$

Table 8

Wavelength of longest waves:	≦ 300 m	> 300 m	
Depth:			
< 100 m	44 (36)	20 (28)	64
100-200 m	12 (20)	23 (15)	35
	56	43	99

$\chi^2 = 11.5,\ P(\chi^2) < 10^{-3}$

Table 9

Depth:	< 100 m	100-200 m	
Season:			
before mid-July	22 (24)	42 (40)	64
after mid-July	15 (13)	20 (22)	35
	37	62	99

$\chi^2 = 0.76,\ 0.25 < P(\chi^2) < 0.5$

depth 134 m, has mean wavelength 990 m. The mean wavelength of the shortest waves is 670 m in midseason, in the second half of July, while the mean value for packets seen earlier or later in the season is 430 m.

9. Dispersion of packets

An internal wave travels on the interface between two layers with phase speed given by (Neumann and Pierson, 1966)

$$c^2 = \frac{g\,\Delta\rho/\rho}{k(\coth kh_1 + \coth kh_2)} \tag{10}$$

For long waves (kh_1 small) this becomes approximately

$$c = c_o \left(1 - \frac{(k^2)\, h_1 h_2}{6} \right) \tag{11}$$

c_o being the limiting phase velocity when kh_1 vanishes. Phase velocity increases with wavelength, approaching the maximum value c_o as wavelength becomes very long compared to depth. The longest waves are expected to lead the packet, and the shortest to bring up the rear, and this is in fact the most frequent case observed among internal-wave packets, as Apel et al. (1975a) pointed out. A considerable proportion (15%) of packets, however, show the opposite arrangement, with slick spacing increasing toward the rear, while another group, comprising 24% of the packets, have almost uniform wavelength throughout. The configuration is not dependent simply on topography, for both normally dispersed and anomalous or slightly dispersed packets are sometimes observed at the same location. The effect of shoaling, with leading waves entering shallow water and being slowed earlier than the trailing waves, offers a qualitative explanation which turns out to be quantitatively inadequate: the depth does not vary sufficiently over the extent of a packet. On the other hand, the anomalously dispersed packets show a predilection for long wavelength and for shallow water. Contingency analysis shows normal dispersion related to large kH with probability of chance occurrence less than one in a hundred. The anomalously dispersed packets have smaller difference in slick spacing or wavelength within the packet than the normally dispersed packets do, that is, they are closer to having uniform spacing. The difference between the longest and shortest wavelength in the packet being $\Delta\lambda$, and the mean value $\bar{\lambda}$, the mean value of $\Delta\lambda/\bar{\lambda}$ is 0.52 for normally dispersed packets, and 0.36 for packets with longer wavelengths in the rear.

10. Comparison of observed dispersion to linear dispersion; breaking

As a rough estimate of wave speed we have used the long-wave limit (7) in which the ratio of amplitude to depth and the ratio of depth to wavelength are assumed to be small, and terms in a/H and k^2H^2 are neglected. In the long-wave approximation (11) terms in $(kH)^2$ are retained, but not higher powers of kH, nor amplitude terms, $\frac{a}{H}$. To this approximation, the longest and shortest waves in a packet, with wave numbers k_1 and k_2, have speeds differing by

$$\Delta c = c_o \, (k_2^2 - k_1^2) \, \frac{h_1 h_2}{6}.$$

With typical values $\lambda_1 = 1000$ m, $\lambda_2 = 300$ m, $h_1 = 60$ m, $h_2 = 40$ m, $\frac{\Delta c}{c_o} = 0.16 = \frac{\Delta d}{d}$, where d is the interpacket separation corresponding to one tidal cycle and Δd is the increase in extent of the packet during this period. With d = 26 km, we expect $\Delta d = 4$ km, yet observe the packets to maintain the same extent of about 2.5 km over two or more cycles. The observed dispersion is considerably less than expected for linear dispersion of waves of the observed wavelength. Gargett (1976) drew the same conclusion for internal waves observed in the Strait of Georgia.

A more detailed analysis of individual packets avoids some uncertainties in this estimate. The long-wave approximation can be avoided by use of the expression (10) for phase velocity, which, with $c = \omega/k$, permits calculation of the group velocity $c_g = d\omega/dk$. The shoaling effect, which tends to counteract dispersion, can be included explicitly. Treating packets as linear dispersive waves, we calculate for the leading wave and for a later wave (say the 5th wave) the group velocity

$$c_g = \frac{c}{2} \, \frac{(1 + kh_1/\sinh^2 kh_1 + kh_2/\sinh^2 kh_2)}{\coth kh_1 + \coth kh_2}.$$

In each of two packets of a series, wavelength for the first and fifth waves was measured as the distance to the next slick. The total depth $(h_1 + h_2)$ was determined for each wave from the bathymetric chart on which the satellite images were overlaid, and the depth h_2 of the upper layer was taken to be 40 m. Then the value of the group velocity was found for each wave, using a constant arbitrary value of $\Delta\rho/\rho$. The velocity of each was taken to be the

mean of the values for the first (fifth) wave in each packet. In most cases, values were similar in the two packets. Then the difference between the velocities for the two waves, Δc, divided by the velocity c of the first wave can be compared to the change in distance Δd divided by the interpacket distance d. The observed values in Table 10 are smaller than expected in all but 2 of the 9 cases; often they are considerably smaller. Evidently the wave packets, at least those observed, disperse more slowly than linear dispersive theory predicts.

For finite-amplitude long waves (terms in a/H retained, terms in kH neglected) the phase velocity and group velocity are equal and given in a two-layer system without shear flow by

$$c = c_o \left(1 + \frac{3}{2} \frac{(h_1-h_2)}{h_1 h_2} \eta\right)$$

where η is the displacement of the interface, and c_o is the long-wave limit of the phase velocity (7).

The crest travels faster than the node, and the trough more slowly, by the amount $\Delta c = \frac{3}{2} \eta c_o \frac{(h_1-h_2)}{h_1 h_2}$. The time for the wave profile to be distorted so that the leading edge is vertical is

$$\tau = \frac{1}{\Delta c} \frac{\lambda}{4} = \frac{c_o}{\Delta c} \frac{P}{4}$$

where P is the period.

For h_1 = 60 m, and h_2 = 40 m, a moderate value of 5 m for amplitude gives $\frac{\Delta c}{c}$ = 1/16 and τ = 4 P; the wave would break within 4 periods. If c_o = 0.58 m/s, corresponding to interpacket separation of 26 km, and wavelength is 450 m, the period is 13 min, and the wave would break within less than an hour. This is clearly not a good description of the wave packets, which are observed to last two or three tidal cycles.

To summarize the situation: wave packets survive about 30 times longer than the time estimated for a long wave of finite amplitude to break, and they disperse at about one-third the rate predicted for nonlinear dispersive waves. In some packets, the distance between successive slicks increases from front to rear, which suggests that in these packets short waves travel faster than long waves, a reversal of the usual wavelength dependence of velocity.

Table 10

Expected $\frac{\Delta c}{c}$	Observed $\frac{\Delta d}{d}$	Ratio: $\frac{\text{observed}}{\text{expected}}$
0.02	-0.02	-0.7
0.02	0.03	1.2
0.04	0.04	1.0
0.05	0.10	2.1
0.15	0.01	0.08
0.18	0.01	0.05
0.18	0.10	0.56
0.26	0.0025	0.001
0.41	0.18	0.44

Theory has been developed for internal waves with both finite-amplitude and dispersive effects (terms in a/H and in $(kH)^2$) included, by Benjamin (1967) for deep water with a shallow layer, and by Benney (1966) for shallow water. Lee and Beardsley (1977) discuss the shallow-water theory, including shear flow and non-Boussinesq effects, and describe numerical solutions and compare them to ocean and laboratory measurements. The dispersion relation is the Korteweg-de Vries equation:

$$\eta_t + c_o \eta_x - \frac{3}{2} \frac{(h_1-h_2)}{h_1 h_2} c_o \eta\eta_x + \frac{h_1 h_2}{6} c_o \eta_{xxx} = 0$$

which has the exact solution:

$$\eta = a(\alpha^2 - 2cn^2 X)$$

where the elliptic function cn X = cosϕ when $X = \int_o^{\phi} \frac{d\phi}{(1-m^2\sin^2\phi)^{1/2}}$ (fig. 33).

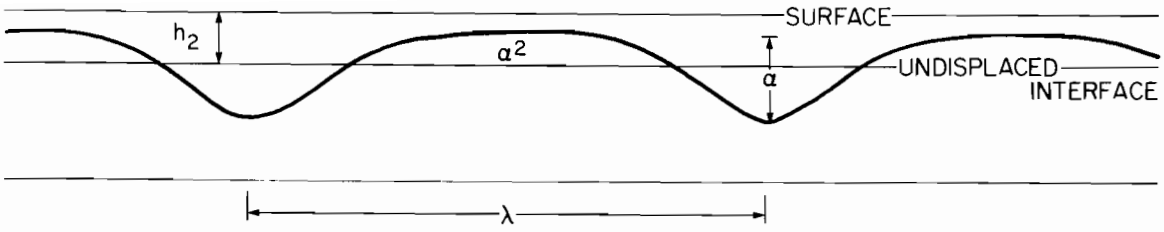

Figure 33. Cnoidal-wave characteristics.

Then $\frac{k_o}{2}\lambda = 2K\,(m^2)$, where $K = \int_o^{\pi/2} \frac{d\phi}{(1-m^2\sin^2\phi)^{\frac{1}{2}}}$

is the complete elliptic integral of the first kind, λ is the wavelength, and k_o is the wave number of the unstretched wave with elliptic parameter $m^2 = 0$. The property of this solution that leads to a wave of permanent form is that the third derivative η_{xxx} contains a term in $\eta\eta_o$ that can balance the nonlinear term in (12):

$$\eta_{xxx} = \eta_x k_o^2 \left(\frac{3m^2\eta}{a} - 1 + m^2(2 - 3\alpha^2)\right) .$$

With this balance

$$m^2 = \frac{3a}{k_o^2} \frac{(h_1-h_2)}{h_1^2 h_2^2} \text{ and } m^2K^2 = a\lambda^2 \frac{3}{16} \frac{(h_1-h_2)}{h_1^2 h_2^2} .$$

Then the wave speed can be expressed in terms of the wave number or the amplitude, or both:

$$c = c_o \left\{1 - \frac{k_o^2 h_1 h_2}{6} [1 - m^2(2 - 3\alpha^2)]\right\}$$

$$= c_o \left\{1 - \frac{a}{2m^2} \frac{(h_1-h_1)}{h\ h_1\ 2} [1 - m^2(2 - 3\alpha^2)]\right\}$$

$$= c_o \left\{1 - \frac{k_o^2 h_1 h_2}{6} + \frac{a}{2} \frac{(h_1-h_2)}{h_1 h_2}(2 - 3\alpha^2)\right\}$$

$$= c_o \left\{1 + D + A\right\} .$$

The first form shows that when m^2 approaches 0, (the wave form becomes sinusoidal), the wave speed approaches the long-wave approximation for linear dispersive waves, while the second form is appropriate for a solitary wave with $\eta = a(\alpha^2 - \text{sech}^2 X)$, $m^2 = 1$ and mean level $\alpha^2 = 0$. The third and fourth forms emphasize the interplay of wavelength and amplitude dependence in cnoidal waves.

Figure 34 shows how the ratio of the amplitude-dependent term to the dispersive term depends on the Ursell parameter, $\frac{a\lambda^2}{H^3}$, and on the relative depths of the layers: when the layers are of equal depth, the amplitude dependence disappears and the dispersive term dominates.

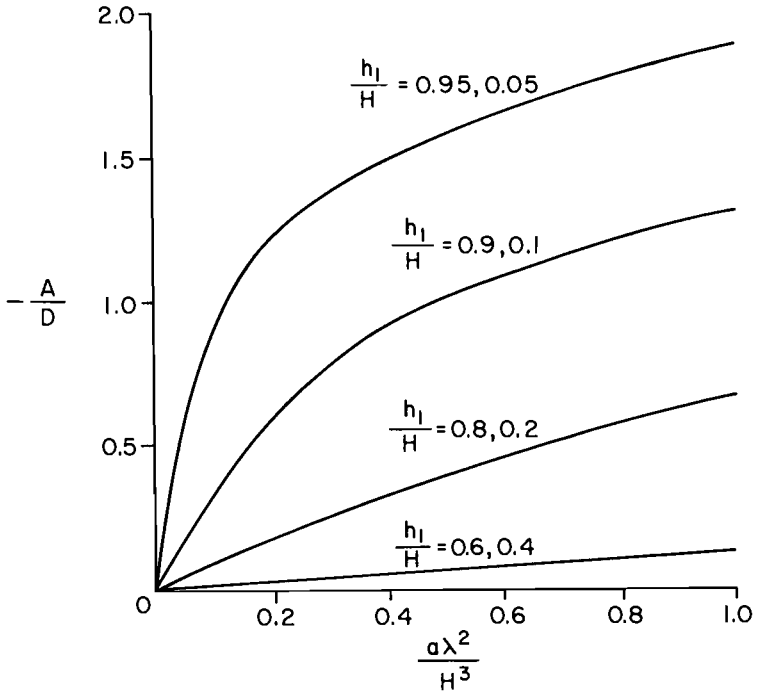

Figure 34. Magnitude of the amplitude-dependent term relative to that of the dispersive term in the exact cnoidal solution of the Korteweg-de Vries equation in which nonlinear terms vanish, giving a permanent wave profile.

The wave speed, (figure 35) can, for large values of m^2, exceed the long-wave limiting wave speed. This allows the speed of a short wave to exceed that of a long wave. For example, in water depth 60 m, a 180-m wave with $m^2 = 0.989$, has wave speed 12% greater than a long wave (≧ 600 m), which has $c \sim c_o$.

This offers an explanation of anomalously dispersed packets, but has the possibly unrealistic feature that the shorter wave would have an amplitude (trough to crest) of 36 m and the long wave a small amplitude of only about 2 m. Of course, a strictly periodic wave train cannot in any case fit the observed variable spacing. If the observations are fit by this type of solution, it would need to include a slow spatial variation of wave number or of the elliptic parameter. The limit to this solution, when the elliptic parameter equals one, is the solitary wave, with profile described by $\mathrm{sech}^2 X$, and with infinitely long wavelength. In this limit, the wave speed is determined by amplitude, and neither changes with time. Considered as a group of solitary waves, a packet could have any type of dispersion, but the pattern would be expected to change quite rapidly, unless all waves had the same amplitude.

11. Tidal phase of generation of internal waves

At least three models have been proposed for the generation of internal waves by tidal currents at the continental slope or at a sill. The tidal phase of generation differs among these models, and so it is of interest to inquire whether this phase can be determined from observations of internal waves and how well the data fit each model.

The first hypothesis is that internal waves are generated by a shearing instability that occurs when velocity shear develops as the barotropic tide generates a baroclinic tide as the density-stratified fluid meets the continental shelf. The Miles-Howard criterion for possible instability is that the Richardson number should be less than ¼:

$$Ri = \frac{g/\rho \frac{d\rho}{dz}}{\left(\frac{\partial u}{\partial z}\right)^2} = \frac{N^2}{\left(\frac{\partial u}{\partial z}\right)^2} < \tfrac{1}{4}$$

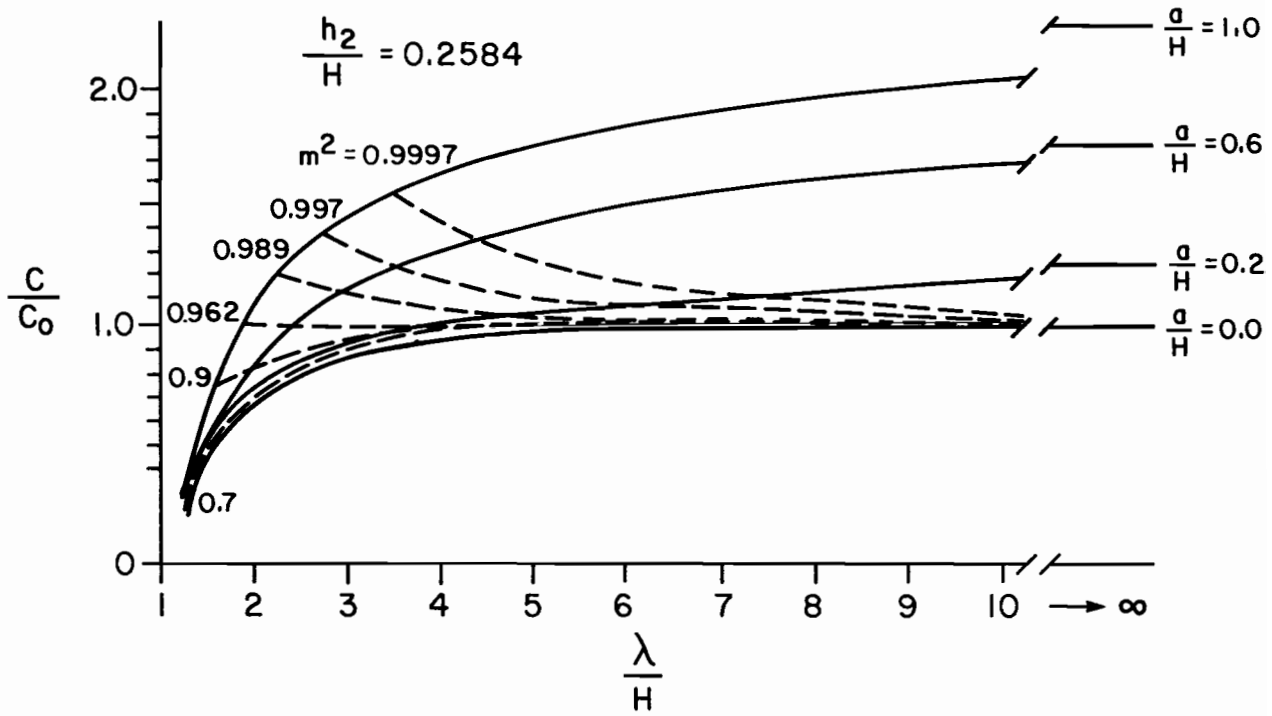

Figure 35. Cnoidal-wave solutions.

where u is the baroclinic flow and N is the buoyancy frequency. Putting N = 0.02 rad/sec (from density profile of Proni et al., see fig. 21) and u = 0.8 ms^{-1}, we find that the vertical distance over which the current velocity changes from the surface value u to a negligible quantity must be less than 20 m to meet this criterion. The density profiles determined by Proni et al. (1977) and by Halpern (1971) each have widths at half maximum of 20 m, and Halpern's velocity profile has a similar vertical scale, but magnitude only half the value assumed in the calculation above. Halpern made exact calculations of the time-varying Richardson number from his velocity-array data and found that it always (but sometimes barely) exceeded ¼ at station T, and speculated that the limits of stability could be surpassed at the upstream generation site.

Tsai (1977), on the basis of a three-layer model of density and velocity stratification, calculated the rate of growth of internal waves, finding that wavelengths of 200 to 300 m and growth times less than an hour correspond to values of vertical shear of 0.05 to 0.06 s^{-1}. With current speed of 0.8 ms^{-1}, this corresponds to vertical scale no greater than 16 m. Wave speed of 0.58 m s^{-1} derived from packet separation then requires $\frac{\Delta\rho}{\rho} \geqq 0.0017$ and $N \geqq 0.032$. These thresholds are most easily attained when current speed is high, so that the period within an hour of the time of maximum current across the shelf seems the most likely time of wave generation in this model.

Lee and Beardsley (1974) studied internal waves generated by flow over a sill, finding that stable waves form downstream of the obstacle and propagate downstream, away from the obstacle. Their laboratory experiments are similar to those of Long (1954), who studied the hydraulic jump forming downstream from a sill, and found that the amplitude of the jump and its distance from the sill increased as mean flow increased. This leads one to expect that the most favorable time for generation of internal waves is at maximum flood current.

The model and experiments of Maxworthy (1979), however, postulate generation of waves soon after maximum ebb flow. On the ebb tide, a depression forms downstream (seaward) of the sill, and as the ebb slacks, the disturbance propagates upstream, over the sill, and continues shoreward.

The data used to test these theories consist of satellite images of 21 series of slick packets near the continental slope. Figure 36 is a photographically enhanced enlargement of part of a Landsat scene, and figure 37 shows tracings of slicks superposed on bathymetric contours. Such tracings show that all of the packet series (and most of the individual packets) are in water less than 200 m deep. Each packet location is described, in a single dimension, in terms of the distance from the 200-m isobath. For each satellite image, the tidal phase was determined by a rather lengthy series of straightforward relationships. Predictions of rotary tidal currents (U. S. Department of Commerce, 1977) relate the phase at various offshore sites to the time of maximum flood at Pollock Rip Channel (F_{PRC}). For each of 17 stations on Georges Bank and Brown's Bank, the phase of the maximum shoreward current (MSC) was noted. This was usually close to maximum flood current and occurred, on the average, one hour later than F_{PRC}, with variance 0.71 hour.

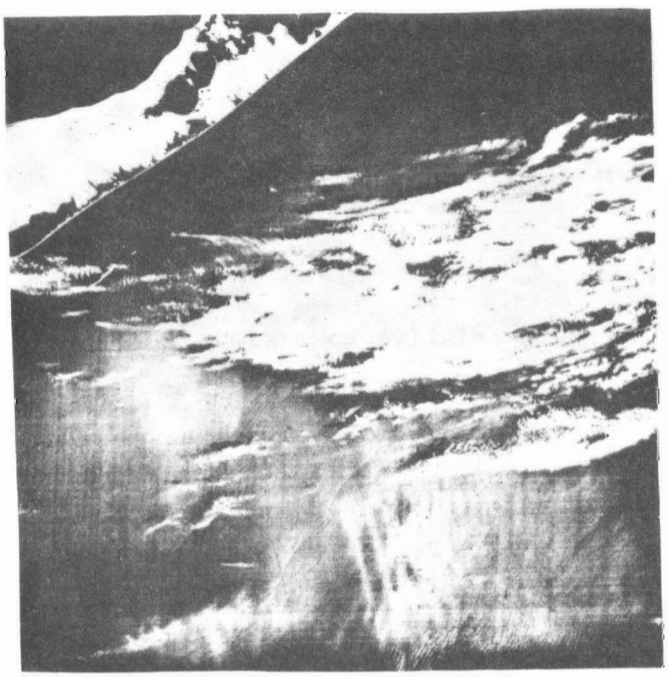

Figure 36. Print, with enhanced contrast, of part of Landsat scene 1365-15013-6, 1973 July 23, showing a series of packets of internal-wave slicks near Hudson Canyon.

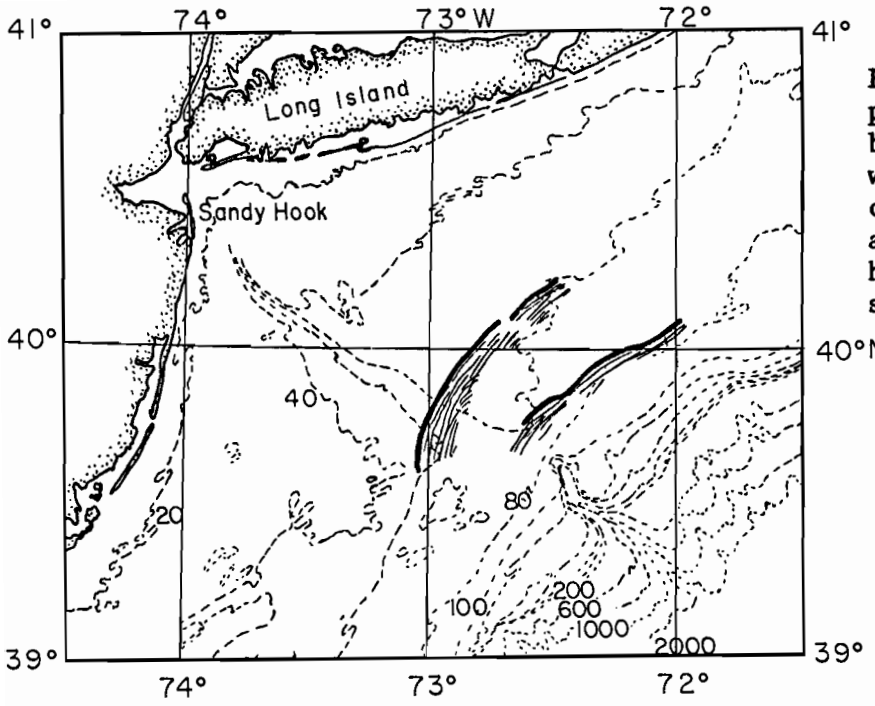

Figure 37. Tracing of packets, superposed on bathymetry. The leading waves of the packets included in the analysis are emphasized with heavier lines in the sketch.

The tidal current tables show the time of maximum flood at Boston Harbor (F_{BH}), which occurs, on the average, 3 hours before high tide at Boston Harbor (HT_{BH}):

$$MSC = F_{PRC} + 1 = F_{BH} - 2.5 + 1 = HT_{BH} - 3 - 2.5 + 1$$
$$= HT_{BH} - 4.5 \text{ hours.}$$

For each image, the phase relative to maximum flood (or to MSC) was determined from the predicted time of high tide at Boston Harbor for that day. In figure 38, the data are plotted, along with curves representing the shoreward progress of wave packets generated on the ebb (dashed curves) or the flood (solid curves) propagating shoreward with constant wave speed and advected by the tide. Distance from the generation site is given by:

$$d(t) = \int_{t_o}^{t} dt'(c - U_o \cos\frac{2\pi t'}{P})$$
$$= c(t-t_o) - \frac{PU_o}{2\pi} \sin\frac{2\pi t}{P} - \sin\frac{2\pi t_o}{P} .$$

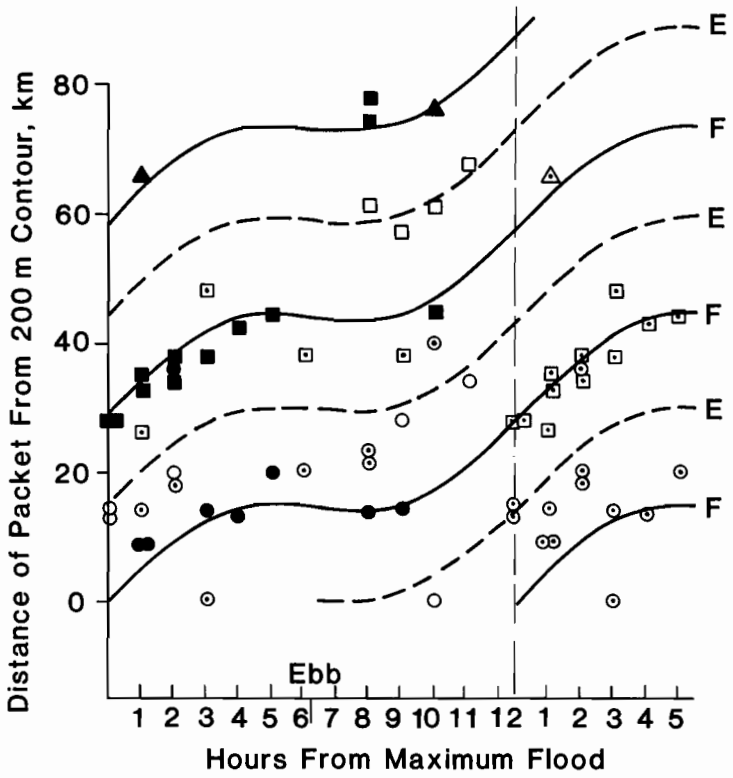

Figure 38. Distance in km of slick packets from the 200-m depth contour plotted against tidal phase at the time of observation. Squares designate second packets in a series and triangles, third packets. The curves show the relation between tidal phase and distance from generation point expected for generation at maximum flood (continuous) and for generation on the ebb, according to Maxworthy's model (dashed). Wave packets move shoreward with time at constant wavespeed 0.653 ms^{-1} and slosh back and forth with tidal currents with amplitude ± 0.8 ms^{-1}.

The amplitude of the tidal current, U_o, is 0.8 ms^{-1}, matching the mean (and median) value of maximum current for stations on Georges Bank. Wave speed is 0.653 ms^{-1}, corresponding to the mean distance of 29.4 km separating packets, and the tidal period 12.5 hours. Agreement of the data with either model was tested in the following way: each data point was classified as lying within $\frac{29.4}{3} = 9.8$ km of the ebb curve, within 9.8 km of the flood curve, or more than 9.8 km from either curve. In the absence of any preferred phase, the probability of falling into each of these classes is 1/3. In fact, 10 data points are closer to the ebb curve, 22 closer to the flood curve, and 11 are distant more than 9.8 km from both curves. The probability of finding from a total of 43 independent points, 22 or more in one class is

$$\sum_{j=22}^{43} \frac{43!}{j!(43-j!)} \left(\frac{1}{3}\right)^{j} \left(\frac{2}{3}\right)^{(43-j)} = 0.0125$$

The data show considerable organization in agreement with the hypothesis that internal waves are generated at near-maximum flood current. Some caution should be used in accepting this result for the following reasons:

(1) The mean value of separation of packets in series was used in constructing the model curves, so that the distances of the 43 packets are not independent, and the probability of chance occurrence of the observed result is underestimated. If the packets in series were perfectly correlated, so that the distance of one packet from the slope determined the distance of all other series members, the number of independent data points would be 21, and the variance would increase by a factor $(43/21)^{\frac{1}{2}} = 1.43$. This increase in variance increases the area under the normal error curve from 0.0125 to 0.058. This latter value may be regarded as an upper limit, since the packets within series are <u>not</u> perfectly correlated. It seems safe to estimate that the result is significant at the 5% level.

(2) The 200-m contour was chosen as the origin of the distance measures. Obviously, if the origin were chosen 15 km (more or less) distant from the unknown site of generation, the points would fit ebb generation, rather than flood generation. This much uncertainty in the origin is unlikely, however, because it would require a 15-km interval of distance devoid of packets or the occurrence of many packets beyond the proposed site of generation. It would also put the source in water of unlikely depth, either shallower than the depth of many packets, or in water 600-1500 m deep, where there is seldom a sudden change in slope. A "corner," such as occurs in many of the profiles of figure 15 at a depth near 200 m, is a likely generation site according to several theories (see Roberts [1975], figs. 2-4).

(3) The use of average relations based on predicted tidal currents and tides probably introduces errors of an hour or two in individual estimates of tidal phase, which results in scattering of the data points. The model curves are based on average values for tidal-current speed and wavespeed, and these values are not accurate in each individual case. An attempt to take into account the variation of wave speed with depth did not improve agreement of observations with the model.

These data have been reanalyzed, using individual wave speeds determined for each packet series from the interpacket separation in that series. The results unambiguously favor generation at flood and will be published separately.

The second set of data used to test the theories is Halpern's observations of thermal oscillations at a site 9 km west of Stellwagen Bank (fig. 39). Here, the time of arrival of internal waves at a fixed location is modeled in terms of waves generated at the flood on the shoreward side of the sill, or near the ebb on the seaward side of the sill (fig. 40). It turns out that either model can fit the data with more or less plausible assumptions. In Lee and Beardsley's numerical model, wavelets on the primary disturbance require a time interval of 98 min to grow to a wavelength of 200 m. The 70-min delay

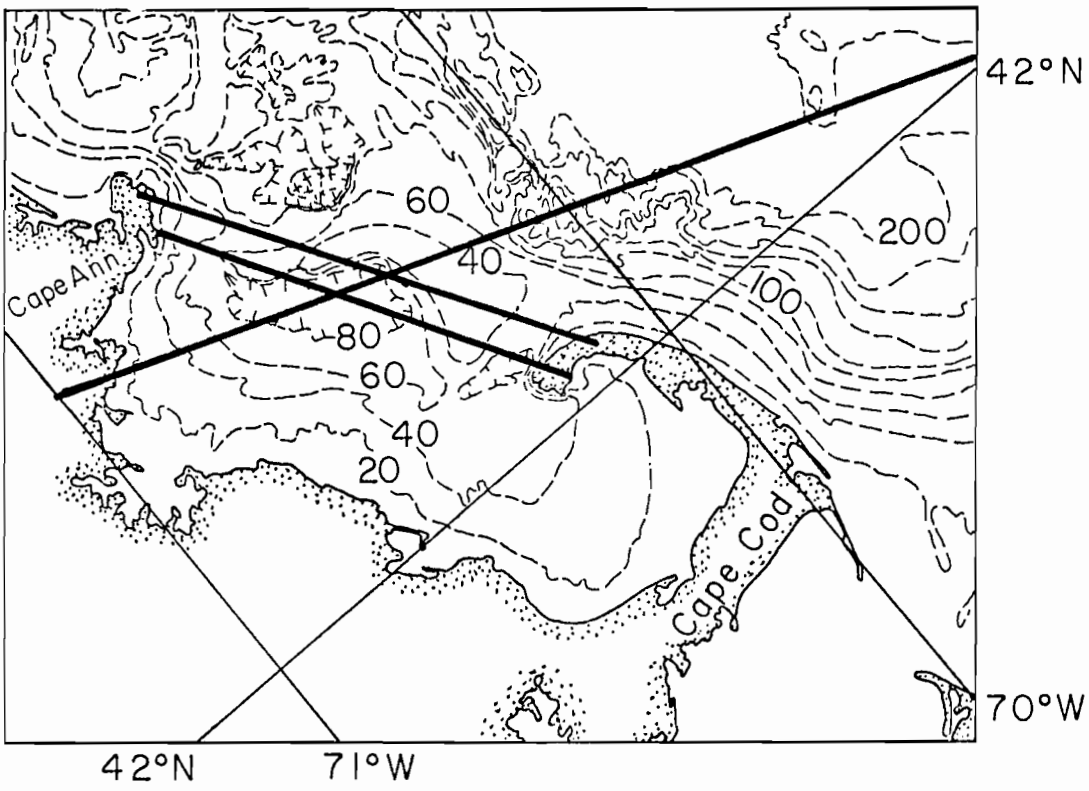

Figure 39. Bottom topography around station, T, the site of Halpern's measurements. The transects correspond to the profiles in figure 40.

from maximum flood to arrival of the waves (with 200-m wavelength) at station T puts the time of generation (the time that wavelets begin to form on an initial long-wavelength disturbance) at 28 min before maximum flood current. The distance covered by waves propagating at C = 0.53 m/s and advected by the tidal current with amplitude U_o is

$$d(t) = \int_{t_o = 28x60}^{t = 70x60} dt'(c+U_o \cos \frac{2\pi t'}{12.5x3600})$$

Distance in km = 5.88 C + 5.63 U_o. Putting U_o = 0.8 ms^{-1} gives d(t) = 7.6 km; alternatively, taking d(t) = 9 km gives U_o = 1.04 m/s. Either of these solutions seems reasonable. In Maxworthy's model, the ebb current flowing over the sill creates a stationary wave on the seaward side of the sill. As the ebb slacks, this wave propagates over the sill and continues shoreward. The

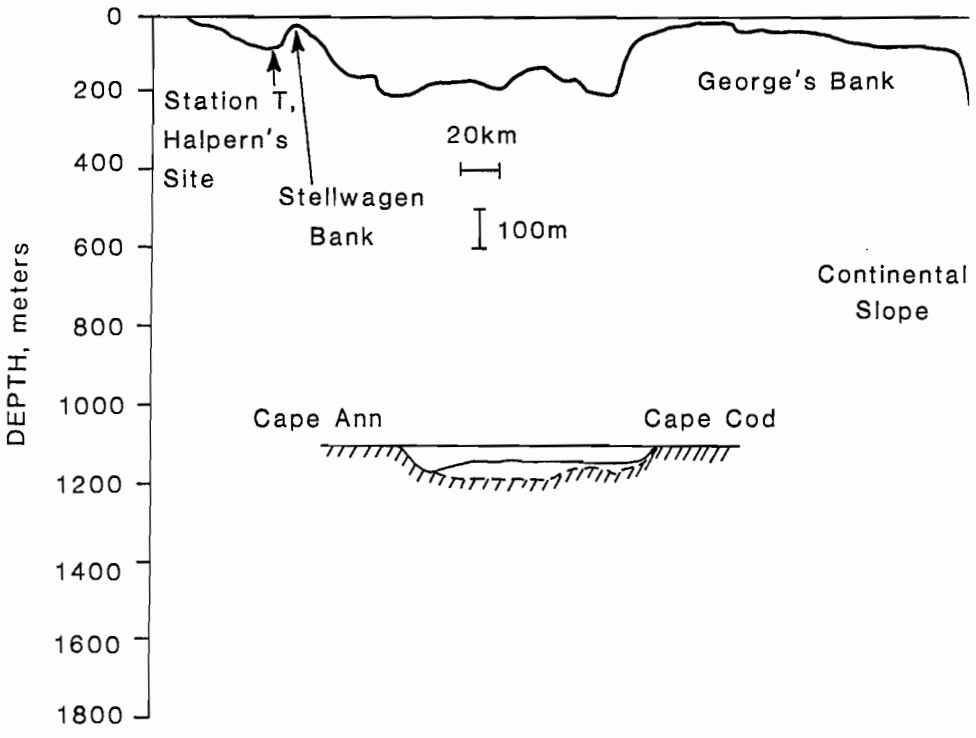

Figure 40. Bottom profile across the continental slope, Georges Bank, Stellwagen Bank, and Halpern's station T. Inset: A bottom profile slightly shoreward of station T, from Cape Ann to Cape Cod. In both profiles, the vertical scale is exaggerated by a factor of 200.

magnitude of the wave speed relative to the amplitude of the tidal current determines how long a period elapses after maximum ebb before the wave is released. The velocity ratio also determines the effective shoreward velocity. If the wave is assumed to start from a location beyond the sill, 15 km from station T, the sets of parameters in Table 11 bring the disturbance to station T 70 min after maximum flood, as observed.

The earlier entries in the table have rather small values of U_o, the tidal-current amplitude, and the later entries have apparent wave speed, U(t)+C, smaller than observed. Nevertheless, the values are not completely unreasonable, and we must conclude that these data fail to eliminate completely either model, though they tend to favor generation near flood.

Table 11

Wave speed c, tidal current amplitude, U_o, time t_o, from maximum ebb to release of wave, and apparent speed at station T.

c, ms^{-1}	U_o, ms^{-1}	t_o, min	$U(70^m)+c$, ms^{-1}
0.52	0.55	40	0.85
0.51	0.60	66	0.76
0.47	0.70	102	0.56
0.43	0.78	118	0.43

Tsai's models show that rapid growth is favored by strong vertical shear of current; the most favorable circumstance combined generation at maximum tidal current (supposing a strong current flowing over the sill produces strong shear) with a long, slow journey from the site of generation to the observation station. If ebb flow is as efficient as flood in producing shear, generation on the ebb would lengthen the travel time to station T, because the generation would be on the seaward side of the sill, adding the crossing of the sill to the distance to be covered, and because seaward advection by the ebb current slows shoreward progress of the waves. The problem of generating

waves that would arrive at station T at the observed phase of the tidal cycle and with the observed speed is the same as for Maxworthy's model, discussed above. The Tsai-Apel model adds only the consideration that long travel time, a characteristic of ebb-generated waves, permits slower growth rate and less extreme shear.

We conclude that tidal advection must be taken into account in analyzing the motions of wave packets over periods that are not complete tidal cycles, and that both Halpern's observations and our data on internal-wave slicks favor generation on the flood, though not decisively.

12. Acknowledgements

Many of the measurements described in this report were made at the Atlantic Oceanographic and Meteorological Laboratory. The technique of comparing satellite images and bathymetric charts was developed by John Apel. I am grateful to Rudolf Preisendorfer for helpful advice and to Frank Gonzalez for useful discussion on wave solutions and for introducing me to the classic paper of Korteweg and de Vries.

Edward Cokelet deserves special thanks for his careful reading and criticism of the manuscript, as does Jean Chatfield for editing the manuscript and organizing illustrations in the author's absence.

13. References

Apel, J., R.L. Charnell, and R. Blackwell (1974): Ocean internal waves off the North American and African coasts from ERTS-1. Proc. 9th Symp. on Remote Sensing, Univ. Mich. Press.

Apel, J., H.M. Byrne, J.R. Proni, and R.L. Charnell (1975a): Observations of oceanic internal and surface waves from the Earth Resources Technology Satellite. J. Geophys. Res., 80, 865-881.

Apel, J.R., J.R. Proni, H.M. Byrne, and R.L. Sellers (1975b): Near-simultaneous observations of intermittent internal waves on the continental shelf from ship and spacecraft. Geophys. Res. Let., 2, (4), 128-131.

Benjamin, T.B. (1967): Internal waves of permanent form in fluids of great depth. J. Fluid Mech., 29 (3), 559-592.

Benney, D.J. (1966): Long non-linear waves in fluid flows. J. Math. & Phys., 45, 52-63.

Cox, C. and W. Munk (1954): Measurement of the roughness of the sea surface from photographs of the sun's glitter. J. Optical Soc. Am., 44, 838-850.

Gargett, A. (1976): Generation of internal waves in the Strait of Georgia, British Columbia. Deep-Sea Res., 23, 17-32.

Gargett, A. and B. Hughes (1972): On the interaction of surface and internal waves. J. Fluid Mech., 52, 179-191.

Garrett, C. and W. Munk (1975): Space-time scales of internal waves: a progress report. J. Geophys. Res., 80, (3), 291-297.

Gulfstream 1973-1975. U.S. Dept. Commerce, NOAA, National Weather Service.

Halpern, D. (1971): Observations on short-period internal waves in Massachusetts Bay. J. Mar. Res., 29, (2), 116-132.

Hughes, B.A. and H.L. Grant (1978): The effect of internal wave on surface wind waves, 1. Experimental measurements. J. Geophys. Res., 83 (C1), 443-454.

Hughes, B.A. (1978): The effect of internal waves on surface wind waves, 2. Theoretical analysis. J. Geophys. Res., 83 (C1), 455-465.

LaFond, E. and K. LaFond (1969): Perspectives of slicks, streaks, and internal-wave studies. Bull. Japanese Soc. of Fisheries Oceanog., pp. 49-57. Papers in dedication to Professor Michitaka Uda.

LaFond, E. and K. LaFond (1967): Internal thermal structures in the ocean. J. Hydronautics, 1, 48.

Lee, C.-Y. and R.C. Beardsley (1974): The generation of long nonlinear internal waves in a weakly stratified shear flow. J. Geophys. Res., 79, (3), 453-462.

Long, R. R. (1954): Some aspects of the flow of stratified fluids. II. Experiments with a two-fluid system. Tellus, 6, 97-115.

Longuet-Higgins, M. and R. Stewart (1964): Radiation stresses in water waves; a physical discussion, with applications. Deep-Sea Res., 11, 529-562.

Maxworthy, T. (1979): A note on the internal solitary waves produced by tidal flow over a three-dimensional ridge. J. Geophys. Res., 84, no. C1, 338-346.

Möllo-Christensen, E. and A. Mascarenhas (1979): Heat storage in oceanic upper mixed layer inferred from Landsat data. Science, 203, 653-654.

Neumann, G. and W. Pierson (1966): Principles of physical oceanography. Englewood Cliffs, N.J.: Prentice-Hall, Inc.

Proni, J.R., J.R. Apel, H.M. Byrne, R.L. Sellers, and F.C. Newman (1978): Oceanic internal waves from ship, aircraft, and spacecraft: a report on the New York-to-Bermuda remote sensing experiment. U.S. Dept. Commerce, NOAA, P.M.E.L. report.

Roberts, J. (1975): Internal gravity waves in the ocean. New York: Marcel Dekker, Inc.

Sawyer, C. and J.R. Apel (1977): Satellite images of ocean internal-wave signatures. U.S. Dept. Commerce, NOAA, S/T 2401.

Shepard, F.P., N.F. Marshall, and P.A. McLoughlin (1974): "Internal waves" advancing along submarine canyons. Science, 183, 195-197.

Tsai, J. (1977): Shear-flow instability as a source of internal waves on the continental shelf. Thesis, Dept. of Physics, Univ. of Miami, Florida.

U.S. Dept of Commerce, NOAA, NOS, A65, 1975. Tidal current tables, Atlantic coast of North America.

U.S. Dept. of Commerce, NOAA, NOS. Tide tables, east coast of North and South America, 1972, 1973, and 1974.